Supplementary information

Photochromic single atom Ag/TiO_2 catalysts for selective CO_2 reduction to CH_4

Chaogang Ban,[1,†] Yang Wang,[1,†] Yajie Feng,[1] Zhouhao Zhu,[1] Youyu Duan,[1] Jiangping Ma,[1] Xu Zhang,[5] Xue Liu,[1] Kai Zhou,[7] Hanjun Zou,[7] Danmei Yu,[2,6] Xiaoping Tao,[1,2] Liyong Gan,[1,2,3,] Guang Han,[2,4,*] Xiaoyuan Zhou[1,2,3,6,*]*

[1] College of Physics and Center of Quantum Materials and Devices, Chongqing University, Chongqing 401331, China

[2] Chongqing Institute of New Energy Storage Materials and Equipment, Chongqing 401120, China

[3] State Key Laboratory of Coal Mine Disaster Dynamics and Control, Chongqing University, Chongqing 400044, China

[4] College of Materials Science and Engineering, Chongqing University, Chongqing 400044, China

[5] Beijing Key Laboratory of Microstructure and Property of Advanced Materials, Beijing University of Technology, Beijing 100024, China

[6] School of Chemistry and Chemical Engineering, Chongqing University, Chongqing 401331, China

[7] Analytical and Testing Center, Chongqing University, Chongqing 401331, China

* E-mails: ganly@cqu.edu.cn; guang.han@cqu.edu.cn; xiaoyuan2013@cqu.edu.cn

† These authors contributed equally to this work

Materials. All reagents were used as received without further purification. Titanium tetrachloride ($TiCl_4$), ethylene glycol (EG), silver nitrate ($AgNO_3$) and sodium sulfate (Na_2SO_4) were purchased from Shanghai Aladdin Bio-Chem Technology Co., LTD. Ammonia solution (28–30 wt%) and ethanol were purchased from Chengdu Kelong Chemical Co., Ltd.

Preparation of TiO_2 nanoparticles. 1 mL $TiCl_4$ and 30 mL EG were mixed and stirred for 30 minutes. Then, 1 mL water was added to the mixed solution and stirred for 10 minutes. Subsequently, the mixed solution was transferred to a 50 mL Teflon lined autoclave and placed in a 150 ℃ oven for 24 h. The hydrothermal products were washed several times and dried overnight at 60 ℃. The obtained hydrothermal products were heated to 500 ℃ and maintained for 6 h.

Materials characterization. To characterize the crystal structures of samples, PANalytical X'pert diffractometer (Cu Kα radiation, λ = 1.5418 Å) was used to record the X-ray diffraction (XRD) data. UV-vis spectroscopy (Shimadzu UV-3600) was used to survey the optical properties of samples with $BaSO_4$ being the reflection sample. The valence states and the composition of photocatalysts were investigated by X-ray photoelectron spectroscopy (XPS, Thermo Fisher Scientific ESCALAB250Xi). Thermo Fisher Scientific Talos F200S transmission electron microscopy (TEM) operated at 200 kV was carried out to investigate the microstructure and morphology of samples. Quadrasorb 2MP full-automatic specific surface aperture analyzer was used to measure the nitrogen adsorption/desorption isotherms. Brunner-Emmet-Teller (BET) method was carried out to get the specific surface area and pore size distribution. Time-resolved photoluminescence spectra were recorded on Fluorescence spectrometer (FLS1000) and the excitation wavelength was 275 nm. Photoluminescence spectra (PL) were obtained by a steady state fluorescence spectrometer (Shimadzu RF-6000) at room temperature. CO temperature-programmed desorption (TPD) experiments were carried out under a N_2 atmosphere in a quartz micro-reactor. The sample (100 mg) was pre-treated in a flow of N_2 (50 mL min^{-1}) at 80 ℃, and then cooled to room temperature with N_2. The 1% CO gas (50 mL min^{-1}) was then introduced with N_2 (50 mL min^{-1}) to adsorb CO for 30 min. Then, the sample was purged with N_2 until the baseline becomes stable. The sample was heated to 550 ℃. The CO signal was monitored over Thermo Scientific spectrometer (Nicolet iS10, Thermo Corp). Electron paramagnetic resonance (EPR) spectroscopy spectra were measured on Chinainstru&Quantumtech (Hefei) EPR200-Plus with continues-wave X band frequency.

Aberration corrected-HAADF-STEM. AC-HAADF-STEM and energy-dispersive X-ray spectroscopy (EDS) experiments were performed on a Titan Themis G2 transmission electron microscope operated at 300 kV, equipped with a probe spherical aberration corrector. Before the characterization, the sample was ultrasonically dispersed in ethanol for 30 min, and then 40 μl of suspension was dropped on a copper TEM grid coated with a thin holey carbon film and dried at 60 ℃.

XAFS measurements. X-ray absorption fine structure spectra (Ag K-edge) were collected at beamline BL44B2 at the SPring-8 synchrotron in Japan. The storage ring of SPring-8 was operated at 8.0 GeV with a maximum current of 250 mA. Using Si (111) double-crystal monochromatic, data collection was carried out in transmission mode using ionization chamber. All spectra were collected in ambient condition. The acquired EXAFS data was processed according to the standard procedures using the ATHENA module implemented in the IFEFFIT software packages[1]. The k^3-weighted EXAFS spectra were obtained by subtracting the post-edge background from the overall absorption and then normalized with respect to the edge-jump step. Subsequently, k^3-weighted $\chi(k)$ data of Ag K-edge was Fourier transformed to real (R) space using a hanging window (dk = 1.0 $Å^{-1}$) to separate the EXAFS contributions from different coordination shells. To obtain the quantitative structural parameters around central atoms, least-squares curve parameter fitting was performed using the ARTEMIS module of IFEFFIT software packages[2, 3].

DRIFTS for CO adsorption. CO adsorption was collected on a Shimadzu IRTracer-100 with HARRICK diffuse reflection accessory and an *in situ* high temperature reaction chamber. The reaction chamber was swept with Ar (30 mL/min) at 300 K for 30 minutes after loading the samples and then measured to record background spectra. Then, the samples were exposed to CO (1% CO in Ar) for 60 min until saturation. Next, the reaction chamber was swept with Ar for 20 min to remove the CO in the gas phase. The final spectra were obtained with the background spectra removed.

***In situ* DRIFTS for CO_2 photoreduction.** The reaction chamber was swept with Ar (30 mL/min) for 30 min after loading the samples and then heated to 500 K and maintained for 30 min. After cooling to 298 K, the background spectrum was recorded. Subsequently, the CO_2 (10 mL/min) saturated by water vapor was fed into the reaction chamber and continuous spectral recording was

performed. After 10 minutes of feeding, the gas valve was closed and adsorbed under closed conditions for 20 minutes to continue recording the spectra. At the end of adsorption, the spectra were recorded for another 30 min under the illumination of a 300 W Xe lamp.

Measurement details of ultraviolet-visible diffuse reflection spectra (UV–vis DRS), time-resolved photoluminescence spectra (TRPL) and steady-state photoluminescence spectra (PL). In order to avoid the influence of oxygen, the measurements of ultraviolet-visible diffuse reflection spectra (UV–vis DRS), time-resolved photoluminescence spectra (TRPL) and steady-state photoluminescence spectra (PL) were performed by a quasi *in situ* method in a sealed deoxygenated screw-top cuvette. Firstly, 2 mg catalyst powder was uniformly dispersed in 1 mL ultrapure water by ultrasonic. Then, 100 μL resultant suspensions were injected into a screw-top cuvette (Supplementary Fig. S28a) and dried in oven at 60 ℃. After drying, the sample adhered to the inner wall of the screw-top cuvette. Subsequently, the screw-top cuvette was covered by a screw cap, and the oxygen was removed using a vacuum pump and argon gas for multiple cycles. Finally, such obtained screw-top cuvette was placed on the sample stage in PL, TRPL and UV-vis DRS spectroscopy to perform corresponding characterization of the resting-state Ag/TiO_2 (Supplementary Fig. S28b). The screw-top cuvette (Supplementary Fig. S28c) that was illuminated for 20 min was characterized to investigate the active-state Ag/TiO_2. In addition, the excitation and emission wavelengths of TRPL tests are 275 and 465 nm, respectively.

Photoelectrochemical measurement. First, 5 mg catalyst powder was uniformly dispersed in 950 μL ethanol and 50 μL nafion by ultrasonic treatment. Subsequently, 10 μL resulting suspension was dropped onto the glassy carbon electrode and dried naturally. Afterward, Zahner CIMPS-2 electrochemical workstation was used to record electrochemical impedance spectroscopy (EIS), photocurrent and Mott-Schottky plots. A standard three-electrode system was used with 0.5 M Na_2SO_4 as the electrolyte. The working electrode, counter electrode, and reference electrode were glassy carbon electrode with catalyst, Pt foil, and Ag/AgCl, respectively. The electrolytic cell was sealed before test, and argon gas was passed through the electrolytic cell continuously for 30 min to remove oxygen, ensuring that the test was carried out in the absence of oxygen.

Quasi *in situ* XPS. Quasi *in situ* XPS measurements were performed on Thermo Fisher Scientific ESCALAB 250Xi. The instrument contains an analysis chamber, an *in situ* reaction chamber and a preparation chamber. Vacuum degree of analysis chamber was 5×10^{-10} mbar. Optimal energy

resolution and minimum spatial resolution of detector were 0.43 eV and 1 μm, respectively. Ag/TiO_2 XPS spectra were recorded under light irradiation.

Detailed procedures of quasi *in situ* AC-HAADF-STEM. Firstly, the sample was placed into a transparent and sealed container. Then, the container was swept by Ar for 30 min to remove the air and afterward was illuminated for 30 min to get Ag/TiO_2 transformed into active state. Immediately, the resultant active-state sample was transferred to the chamber of aberration corrected transmission electron microscopy. This transfer process was done as fast as possible to ensure the sample was maintained at the active state. Specifically, only ~2 min was spent (see the supplemented video of the process), which is far shorter than the bleaching time (~0.5 h). Subsequently, the active state of Ag/TiO_2 was characterized.

Calculation details. All calculations were performed with the density functional theory (DFT) implemented in the Vienna Ab initio Simulation Package.[4, 5] The ion-electron interaction is described by the projector augmented wave potentials.[6] Spin polarized Perdew-Burke-Ernzerhof functional of the generalized gradient approximation was employed to treat the exchange correlation between electrons[7]. According to the testing results (Fig. S29), a plane-wave expansion energy cutoff of 500 eV was adopted, which is sufficient for accurate results.[8, 9] The D3 method with Becke-Johnson damping function was utilized to improve the description of van der Waals interactions. The effective parameter for Coulomb interaction correction of Ti atom was set to be 6.8 eV, which has been evaluated by comparing the band gap between the theoretical (3.16 eV) and experimental (3.23 eV) value for anatase bulk TiO_2.[10] According to the testing calculations of the slab thickness, i.e. the number of O-Ti-O layer (Fig. S30), the TiO_2 (101) surface was modeled using a slab consisting of two O-Ti-O layers, which is sufficient for accurate results, and a (2 × 3) supercell was used. A vacuum slab of 20 Å thickness along the *c* direction was applied to separate the interactions between neighboring images. Dipole corrections were applied throughout the calculations.[5] The Γ-centered k-point sampling grid of 3 × 3 × 1 and 5 × 5 × 1 were employed for geometry relaxation and electronic structural calculations, respectively. The convergence standards for energy and residual force were set to be 10^{-5} eV and 0.02 eV/Å, respectively.

To simulate electronic excitation from the resting state to the active state, the occupation-constrained DFT calculations were carried out,[11] in which one electron was placed from the highest occupied band to the lowest unoccupied band. The whole procedures are shown in Fig.

S31. In Step I (from point A to point B), the structure at the ground state was firstly optimized to obtain the total number of electrons (point A), and then, one electron was placed from the highest occupied band to the lowest unoccupied band to obtain the electronic structure of excited state (point B). In Step II (from point B to point C), the structure at the excited state was relaxed (i.e., keep the electronic structure of excited state) to obtain the approximate structure at the excited state (point C). This approach has been used to study the phase change in Ge-Sb-Te alloys[12] and has been verified by time-dependent DFT molecular dynamic simulations.[13] It is found that Ag atoms can modify the local structure of Ag/TiO_2 during the dynamic photochromic process. Such structural modifications are similar to the structural variations induced by electron excitation.[11, 13]

To evaluate the availability of protons during the CO_2 photoreduction, H_2O dissociation was investigated by using the climbing image nudged elastic band method.[14]

The adsorption energies were calculated as

$$E_{ads} = E_{total} - E_{slab} - E_X \quad (1)$$

E_{total} and E_{slab} E_X are calculated energies of surface with and without X adsorbed. E_X is the total energy of total energies of gas-phase species.

For CO_2 photoreduction, the associated free energy change (ΔG) of each step was determined according to a computational hydrogen electrode model proposed by Nørskov et al.,[15] and was calculated by

$$\Delta G = \Delta E + \Delta ZPE - T\Delta S \quad (2)$$

ΔE, ΔZPE and ΔS are total energy, zero-point energy and entropy change relative to the initial state, respectively. ZPE was calculated from the vibrational frequencies, which were obtained by considering the adsorption species and the surface atoms that provide corresponding adsorption sites according to previous studies.[16-18] The entropy was taken from the NIST-JANAF thermodynamics table for gaseous molecules.[19] Temperature (T) was set to be 298.15 K. This method is well-accepted in the photocatalytic CO_2 reduction community.[20-28]

As water is crucial for reactions with multiple proton-coupling-electron-transfer steps, explicit water solvation is considered by using a 4-layer H_2O (Fig. S32), which is sufficient to justify the results.[29-32] In addition, the effect of protons on CO_2 and reaction intermediates is also investigated. As shown in Fig. S33, on both surfaces, the presence of water layers enhances CO_2 adsorption, while the addition of a proton slightly weakens the adsorption, similar to previous

studies.[33-38] As for the other reaction intermediates, it is found that the addition of a proton remarkably enhances the bonding strengths of the electron withdrawing groups (Fig. S24), such as *O and *OH. This may be because extra H atoms in the water layer can be spontaneously separated into solvated protons and excess electrons on the surface.[39, 40] The resultant excess electrons can promote charge transfer to these intermediates, thus strengthening their adsorption.

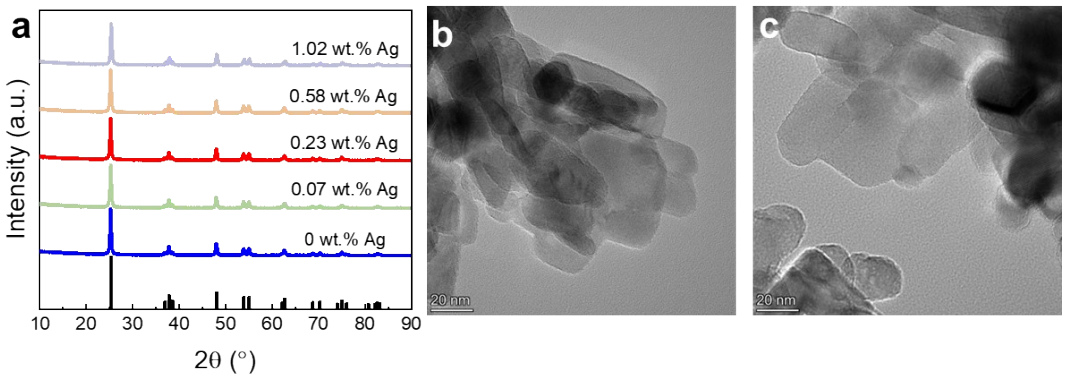

Supplementary Fig. S1. (**a**) XRD patterns of Ag/TiO_2 with different amounts of Ag mass loadings. TEM images of (**b**) TiO_2 and (**c**) Ag/TiO_2 (0.23 wt.%).

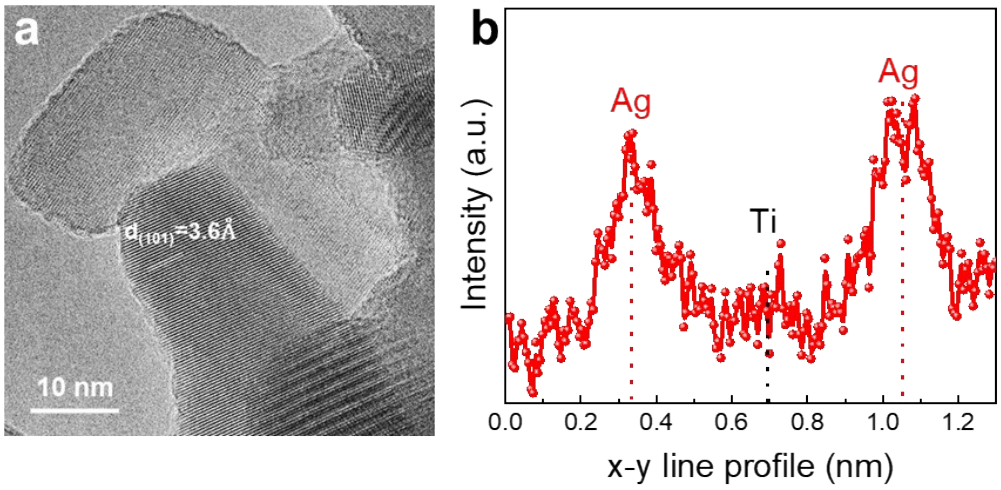

Supplementary Fig. S2. (**a**) HRTEM image of Ag/TiO_2 (0.23 wt.%). (**b**) X–y line scan profile of Ag/TiO_2 (0.23 wt.%), measured from the rectangular region in **Fig. 2a**.

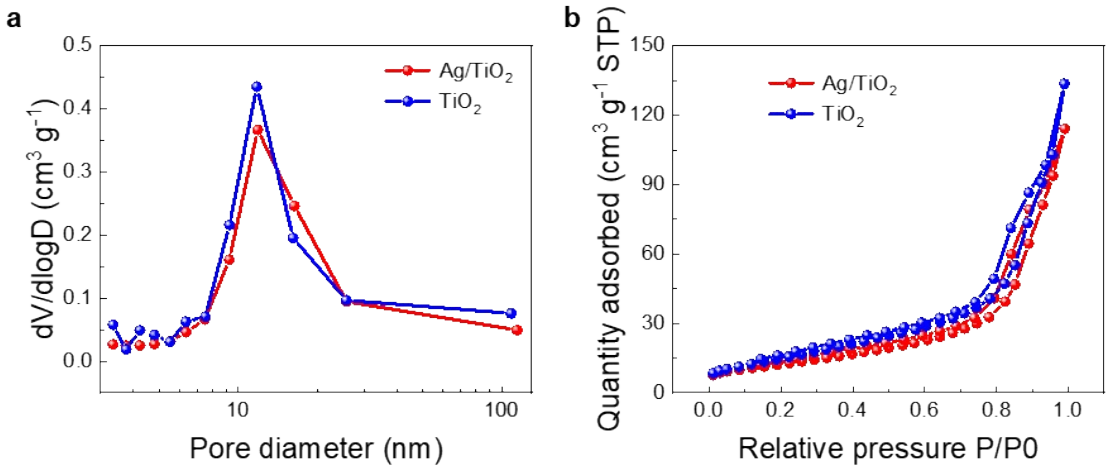

Supplementary Fig. S3. (**a**) Pore size distribution and (**b**) nitrogen adsorption-desorption isotherm curves of TiO_2 and Ag/TiO_2 (0.23 wt.%).

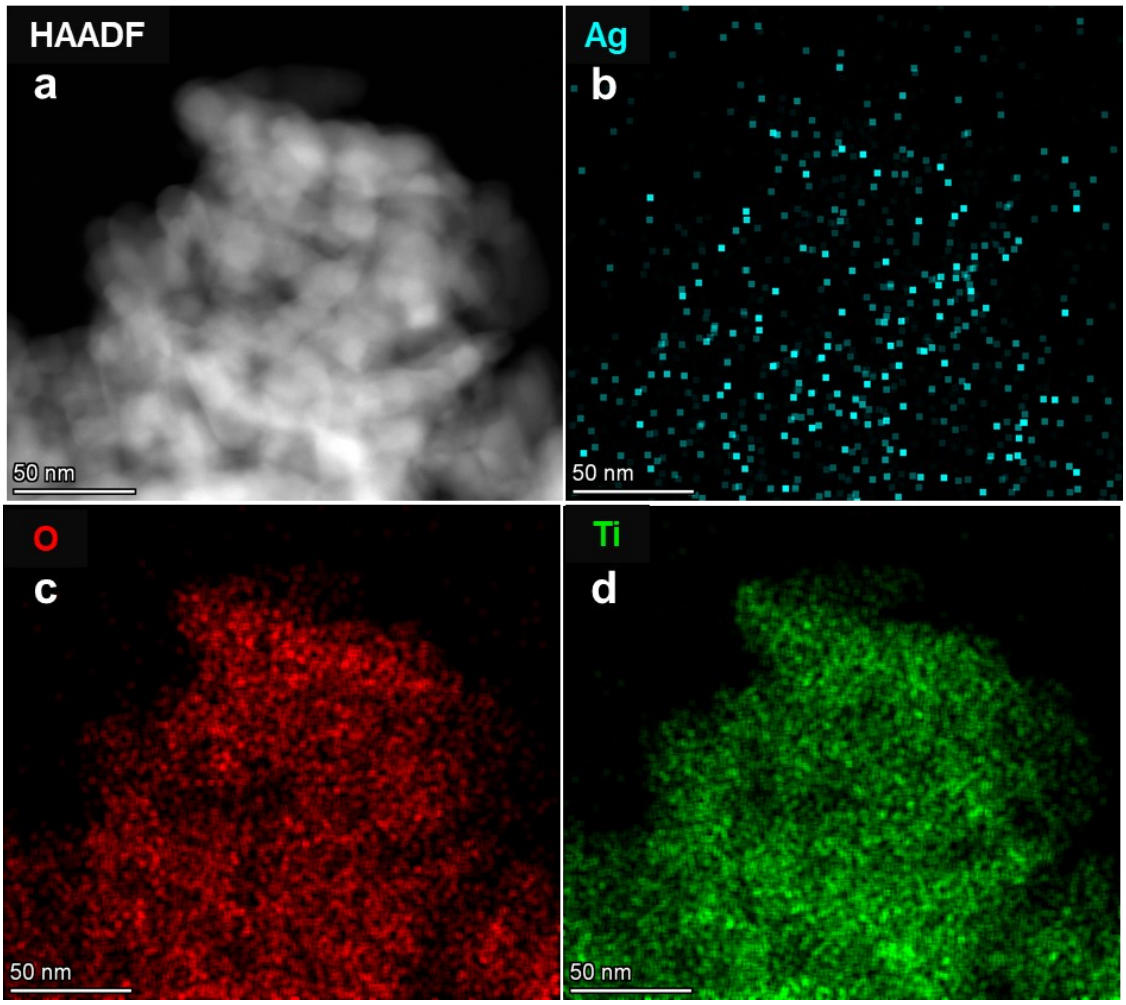

Supplementary Fig. S4. (**a**) HAADF-STEM and (**b-d**) energy dispersive X-ray spectroscopy (EDS) elemental mapping images of Ag/TiO_2 (0.23 wt.%).

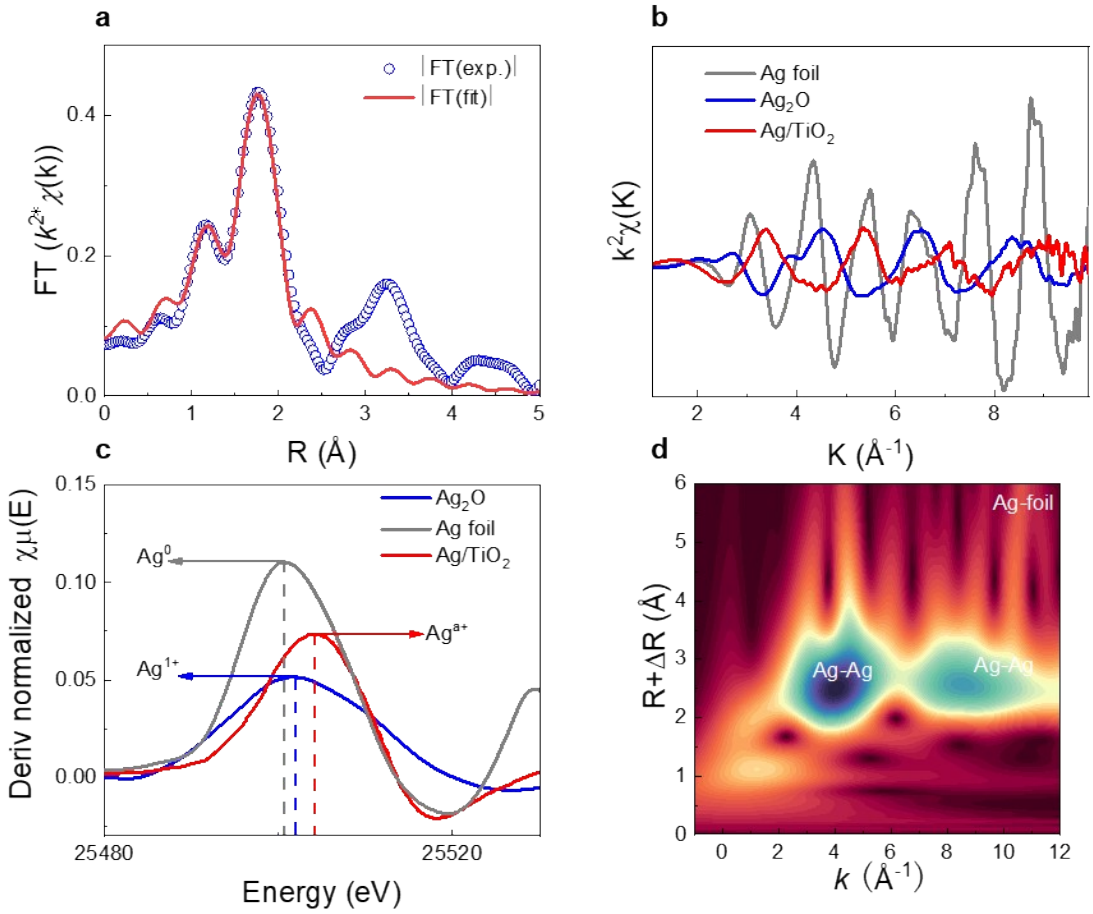

Supplementary Fig. S5. (**a**) EXAFS R space fitting curves of Ag/TiO_2. (**b**) EXAFS k space curves of Ag_2O, Ag and Ag/TiO_2. (**c**) The Ag K-edge XANES first-order differential of Ag_2O, Ag and Ag/TiO_2. (**d**) Wavelet transform of Ag foil.

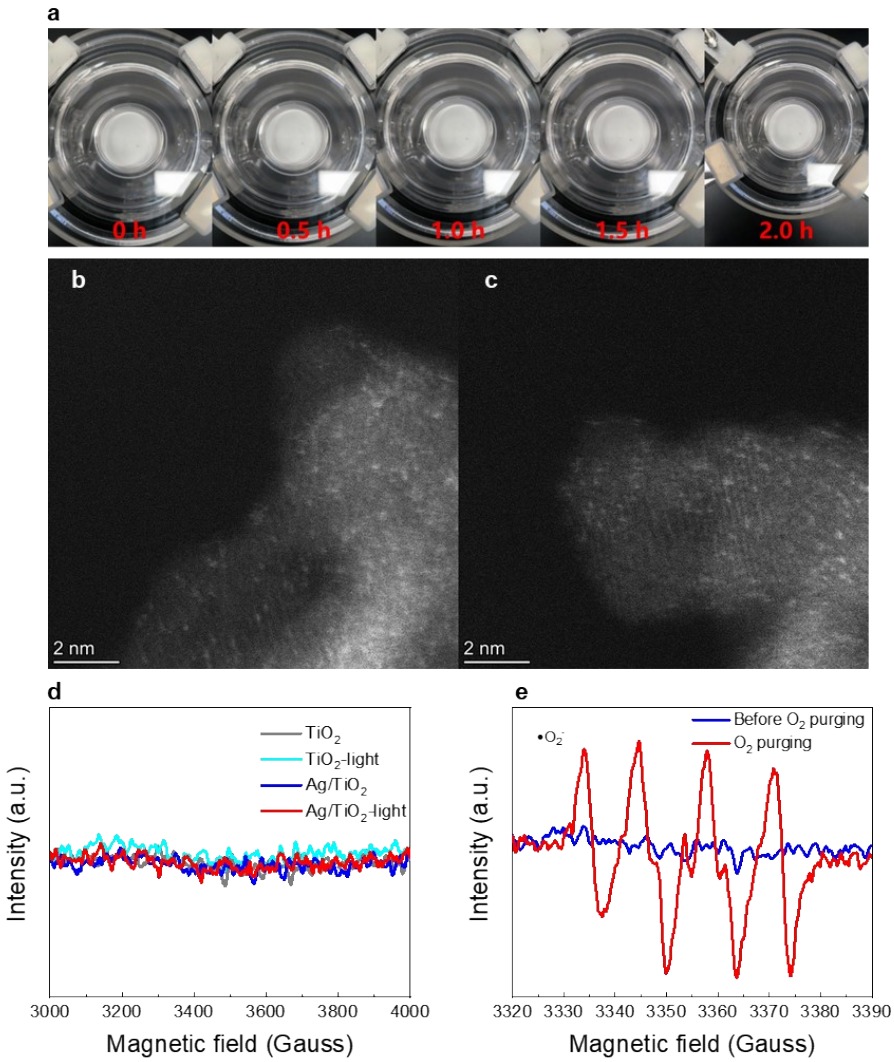

Supplementary Fig. S6. (**a**) Photographs of TiO_2 in different irradiation time (0, 0.5, 1, 1.5 and 2.0 h). The quasi *in situ* AC-HAADF-STEM images of Ag/TiO_2 (**b**) before (resting state) and (**c**) after (active state) light irradiation. *In situ* EPR tests of (**d**) oxygen vacancies in Ag/TiO_2 and TiO_2 under dark and light irradiation and (**e**) $\bullet O_2^-$ over Ag/TiO_2 at the active state before and after O_2 purging.

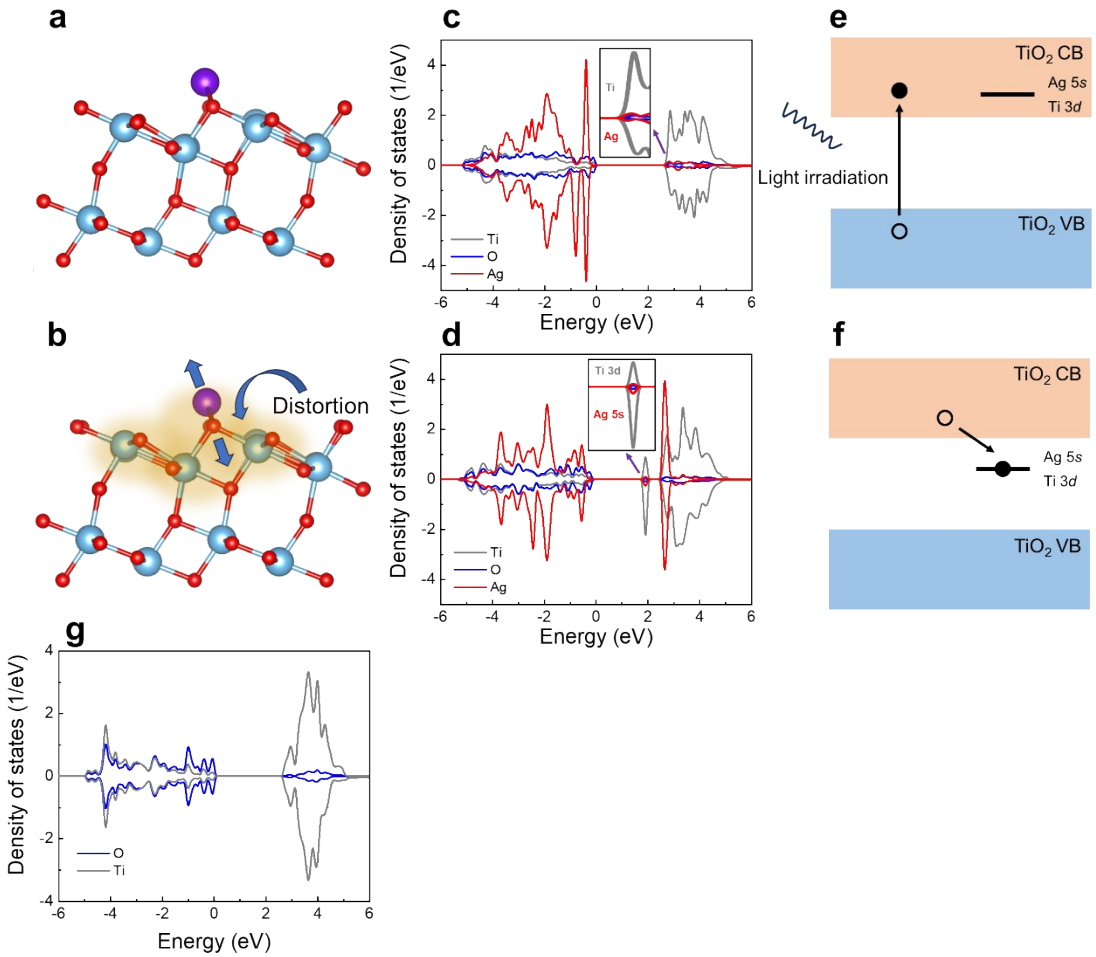

Supplementary Fig. S7. Structure models of Ag/TiO_2 at the (**a**) resting and (**b**) active state. The blue, red and purple balls represent Ti, O and Ag atoms, respectively. Density of states for Ag/TiO_2 at the (**c**) resting and (**d**) active state. Schematics of (**e**) photo-electron generation upon illumination and (**f**) its localization at the mid-gap states. (**g**) Density of state per atom for TiO_2.

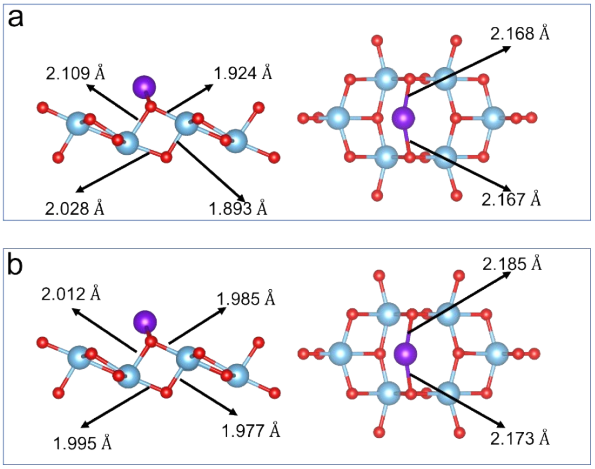

Supplementary Fig. S8. Structural parameters of Ag/TiO_2 at the (**a**) resting and (**b**) active state. The blue, red and purple balls represent Ti, O and Ag atoms, respectively.

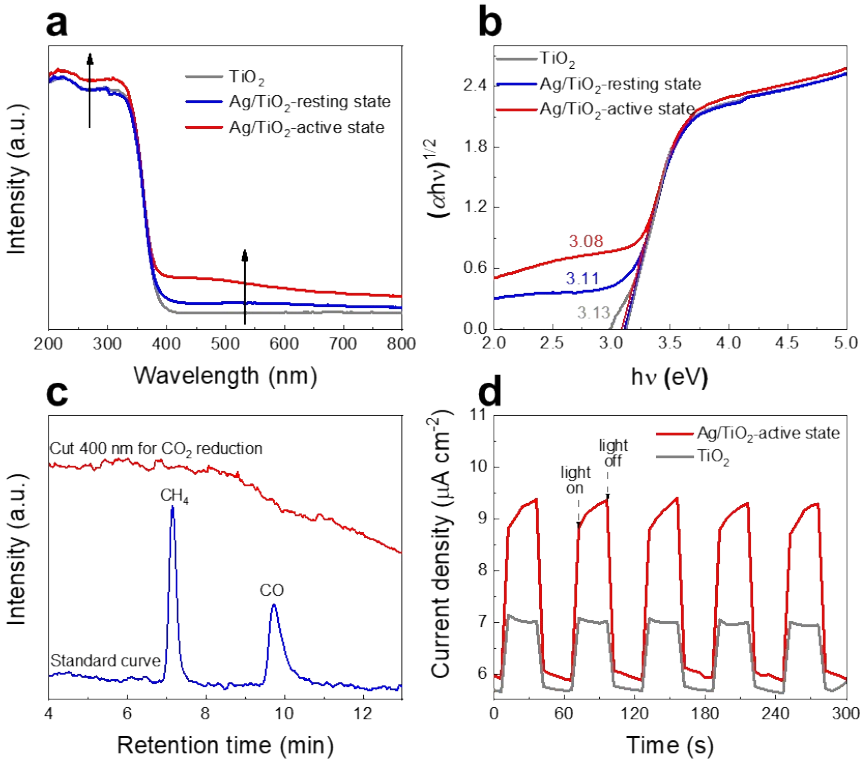

Supplementary Fig. S9. (**a**) UV–vis DRS spectra and (**b**) Tauc plots of the photocatalysts. (**c**) Standard curve (blue) of products from photocatalytic CO_2 reduction and the GC curve obtained from photocatalytic CO_2 reduction on Ag/TiO_2 under a xenon lamp with a 400 nm filter. (**d**) Transient photocurrent responses of TiO_2 and Ag/TiO_2 (0.23 wt.%) at the active state.

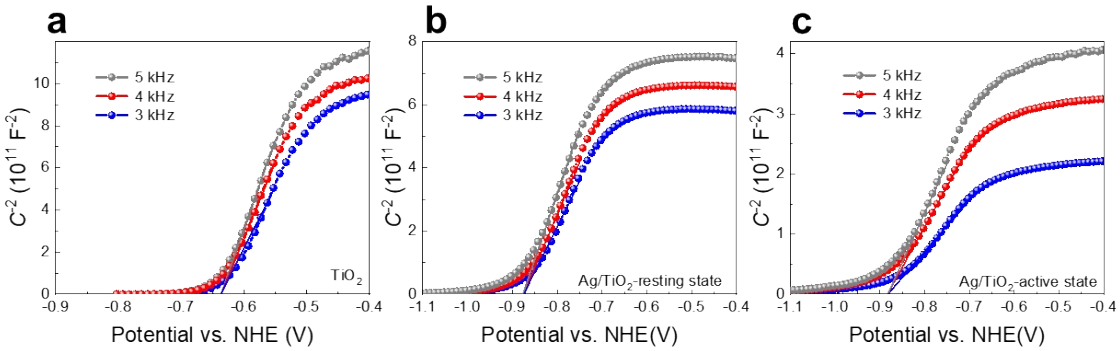

Supplementary Fig. S10. The Mott-Schottky plots of (**a**) TiO_2 and Ag/TiO_2 at the (**b**) resting and (**c**) active state.

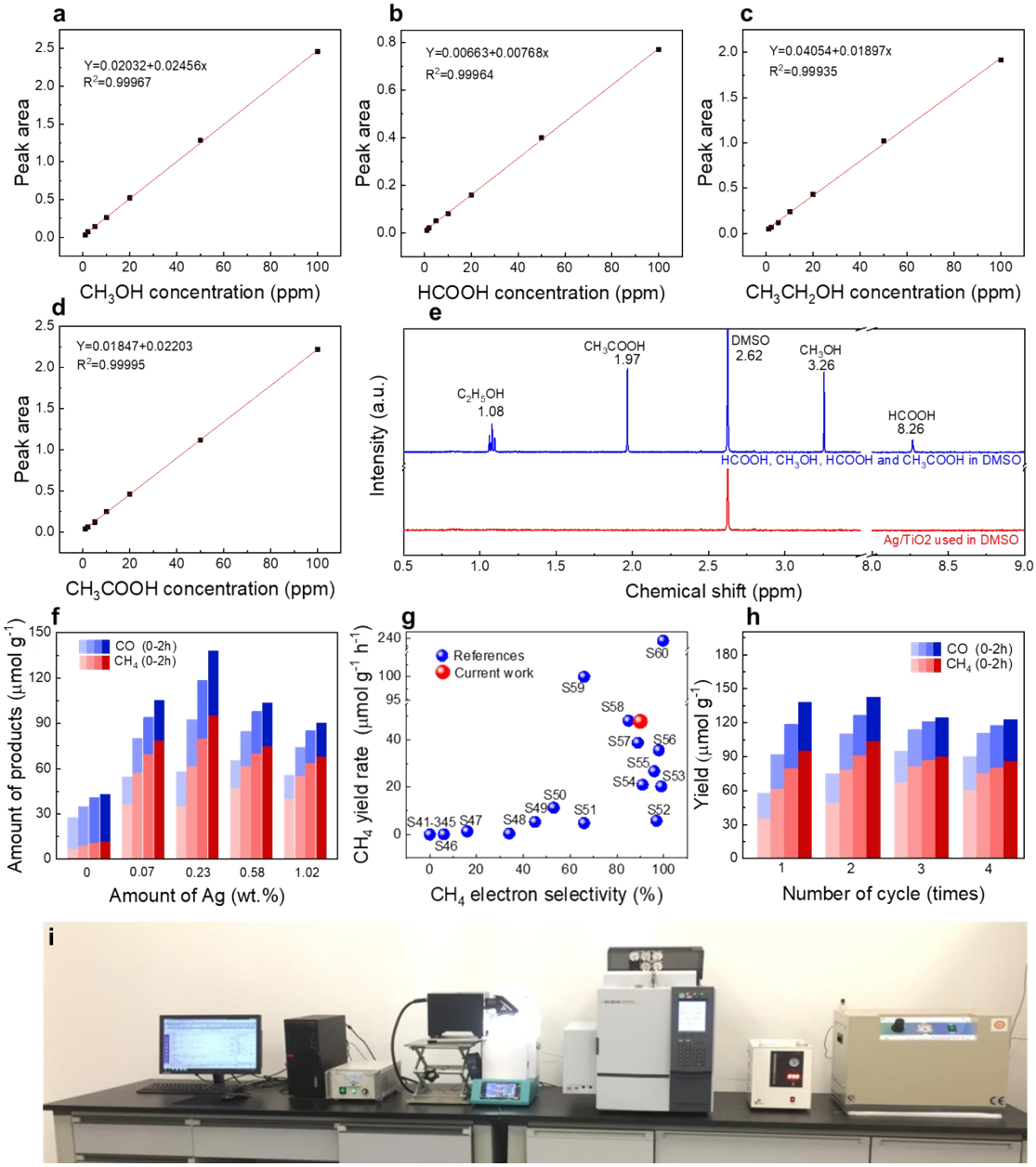

Supplementary Fig. S11. (**a-d**) Standard curves for the measurement of CH_3OH, HCOOH, CH_3CH_2OH and CH_3COOH. (**e**) Standard ^1H NMR spectra of CH_3OH, HCOOH, CH_3CH_2OH and CH_3COOH (blue) and that (red) generated after photocatalytic CO_2 reduction over Ag/TiO_2. (**f**) Performance of photocatalytic CO_2 reduction on Ag/TiO_2 at different Ag mass loadings. (**g**) Comparison of the performance with noble metal decorated photocatalysts in literatures. (**h**) Photocatalytic cycle tests of Ag/TiO_2 (0.23 wt.%), each cycle is 2 hours, every half an hour to take a point. (**i**) A photograph of the test system for photocatalytic CO_2 reduction.

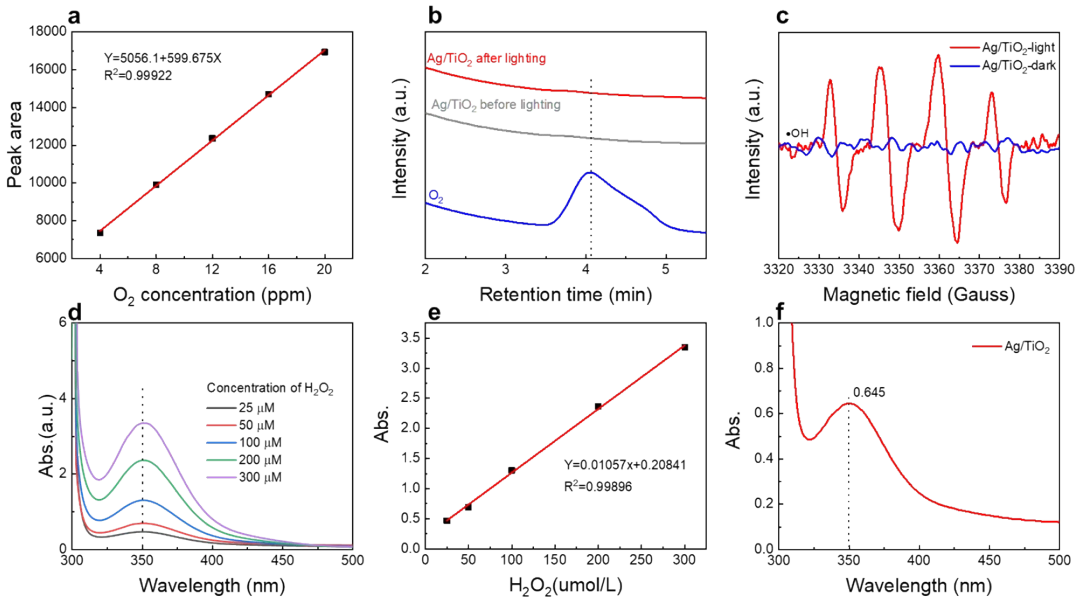

Supplementary Fig. S12. (**a**) Standard curve for the measurement of O_2, and (**b**) the GC spectra of produced O_2 after photocatalytic CO_2 reduction over Ag/TiO_2. (**c**) EPR spectra for •OH for Ag/TiO_2 samples. (**d-e**) Standard curve for the measurement of H_2O_2. (**f**) The UV-vis spectrum of H_2O_2 generated by Ag/TiO_2.

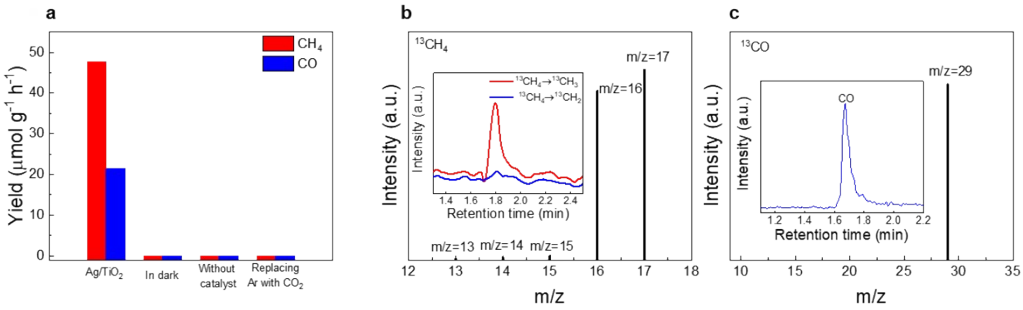

Supplementary Fig. S13. (**a**) Control experiments of photocatalytic CO_2 reduction on Ag/TiO_2 in dark, in the absence of catalyst and in Ar. Mass spectrometer of (**b**) $^{13}CH_4$ and (**c**) ^{13}CO as well as corresponding total ion chromatography (inset) over Ag/TiO_2 using $^{13}CO_2$ as the feedstock.

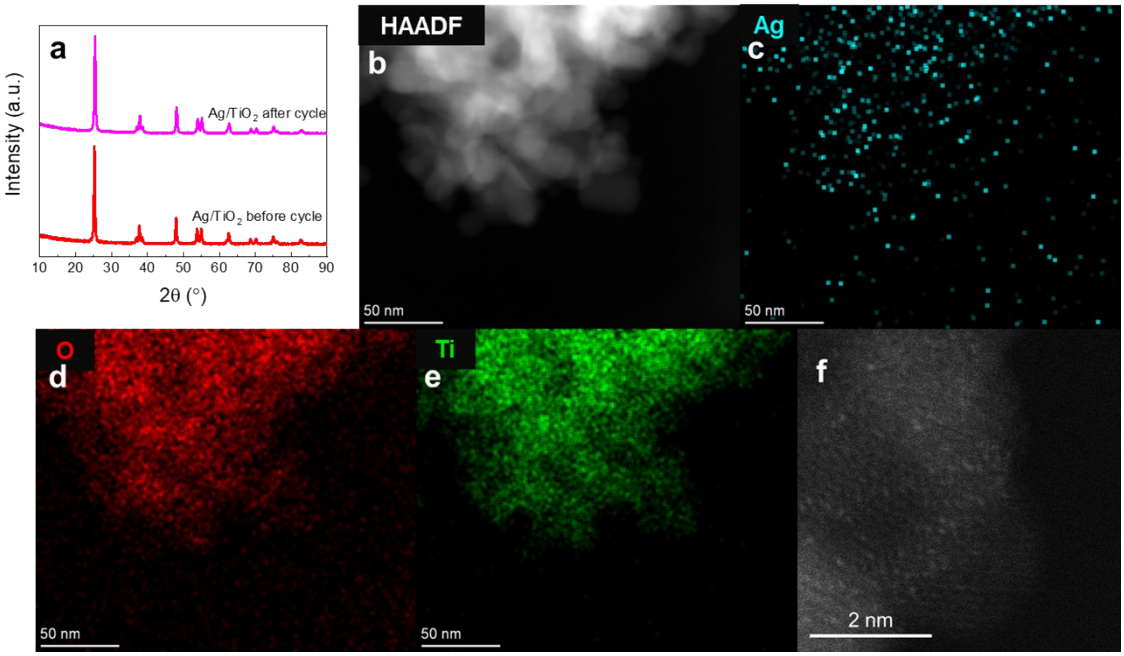

Supplementary Fig. S14. Characterization of Ag/TiO_2 after cycle reactions: (**a**) XRD patterns, (**b**) HAADF-STEM image, (**c-e**) EDS mapping and (**f**) AC-HAADF-STEM images.

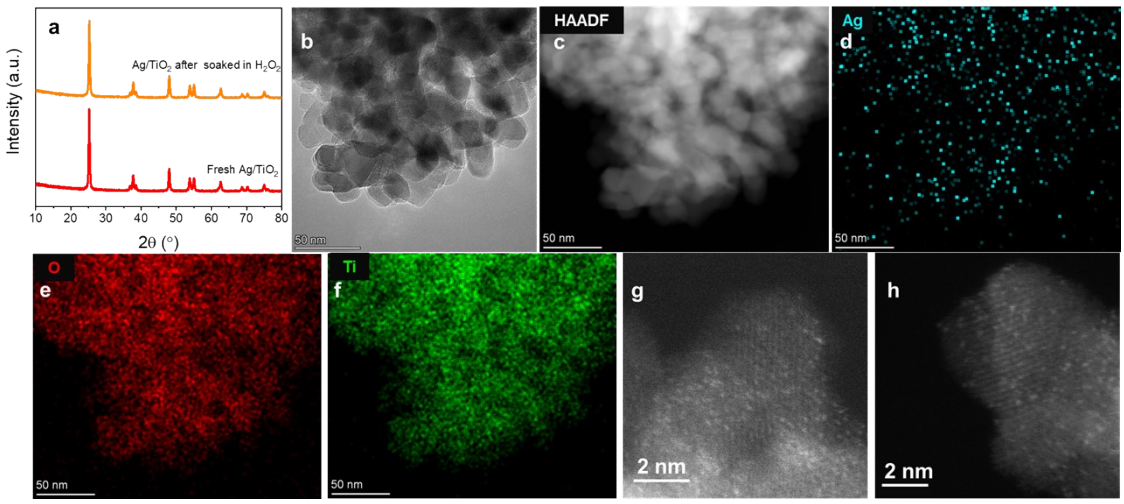

Supplementary Fig. S15. Characterization of Ag/TiO_2 that was soaked in 5 μmol (5 mM) H_2O_2 solution for 2 h: (**a**) XRD patterns, (**b**) HAADF-STEM image, (**c-e**) EDS mapping and (**f**) AC-HAADF-STEM images.

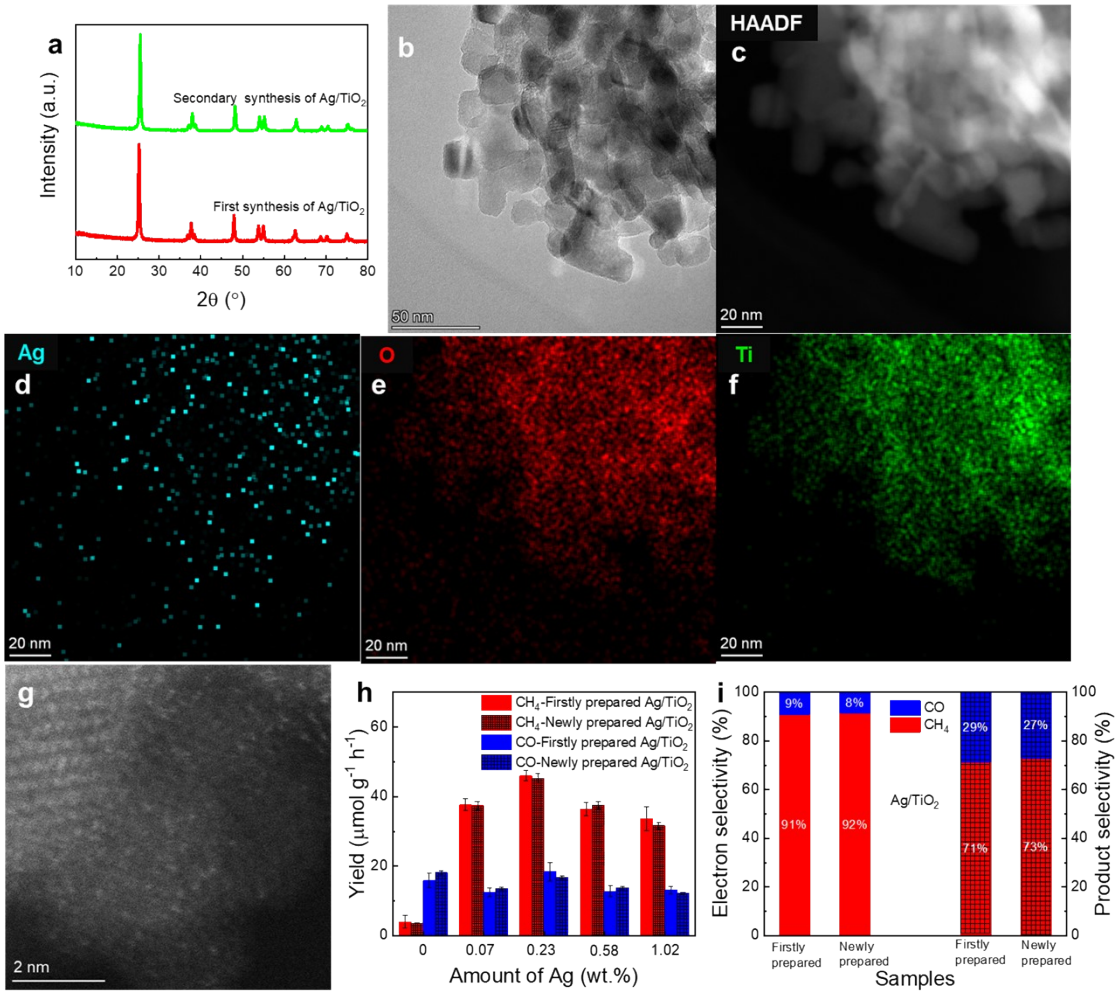

Supplementary Fig. S16. Characterization of the newly prepared Ag/TiO_2 sample. (**a**) XRD patterns, (**b**) TEM image, (**c**) HAADF-STEM image, (**d-f**) EDS mapping and (**g**) AC-HAADF-STEM image. (**h**) Performance and (**i**) electron selectivity comparison between the firstly and newly prepared Ag/TiO_2.

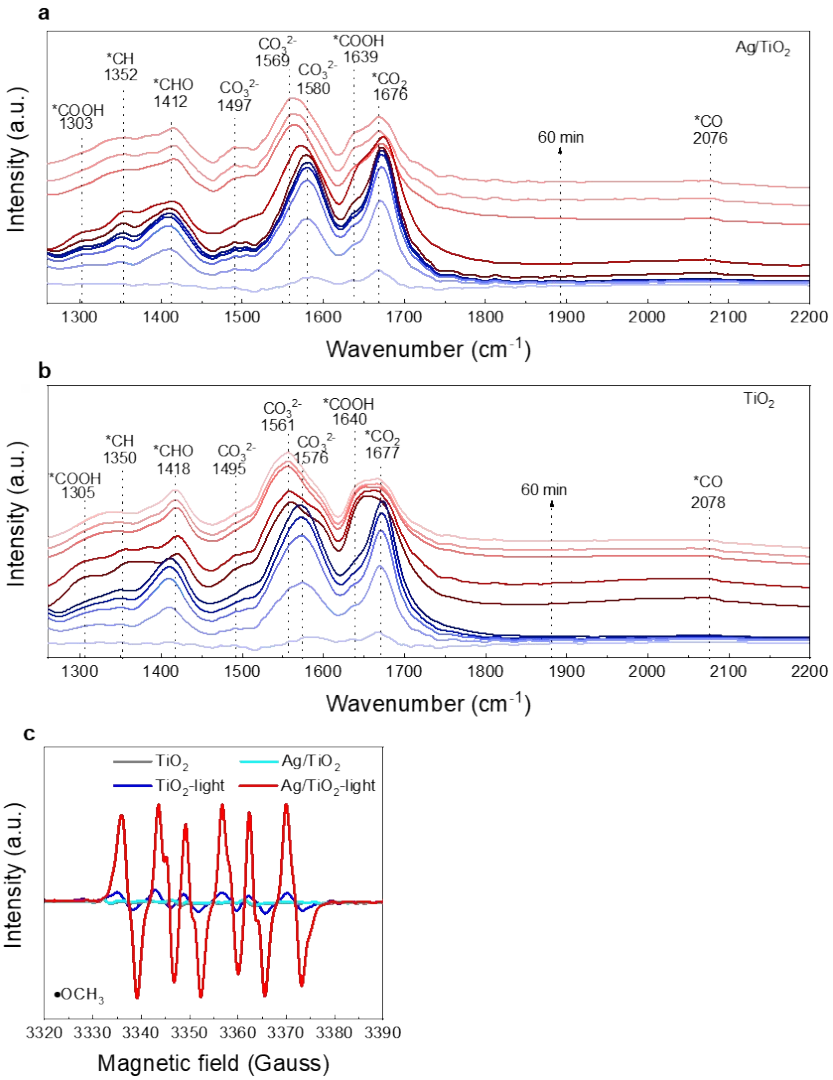

Supplementary Fig. S17. *In situ* DRIFTS of photocatalytic CO_2 reduction on (**a**) Ag/TiO_2 and (**b**) TiO_2. (**c**) *In situ* EPR spectra of $•OCH_3$ signal on TiO_2 and Ag/TiO_2.

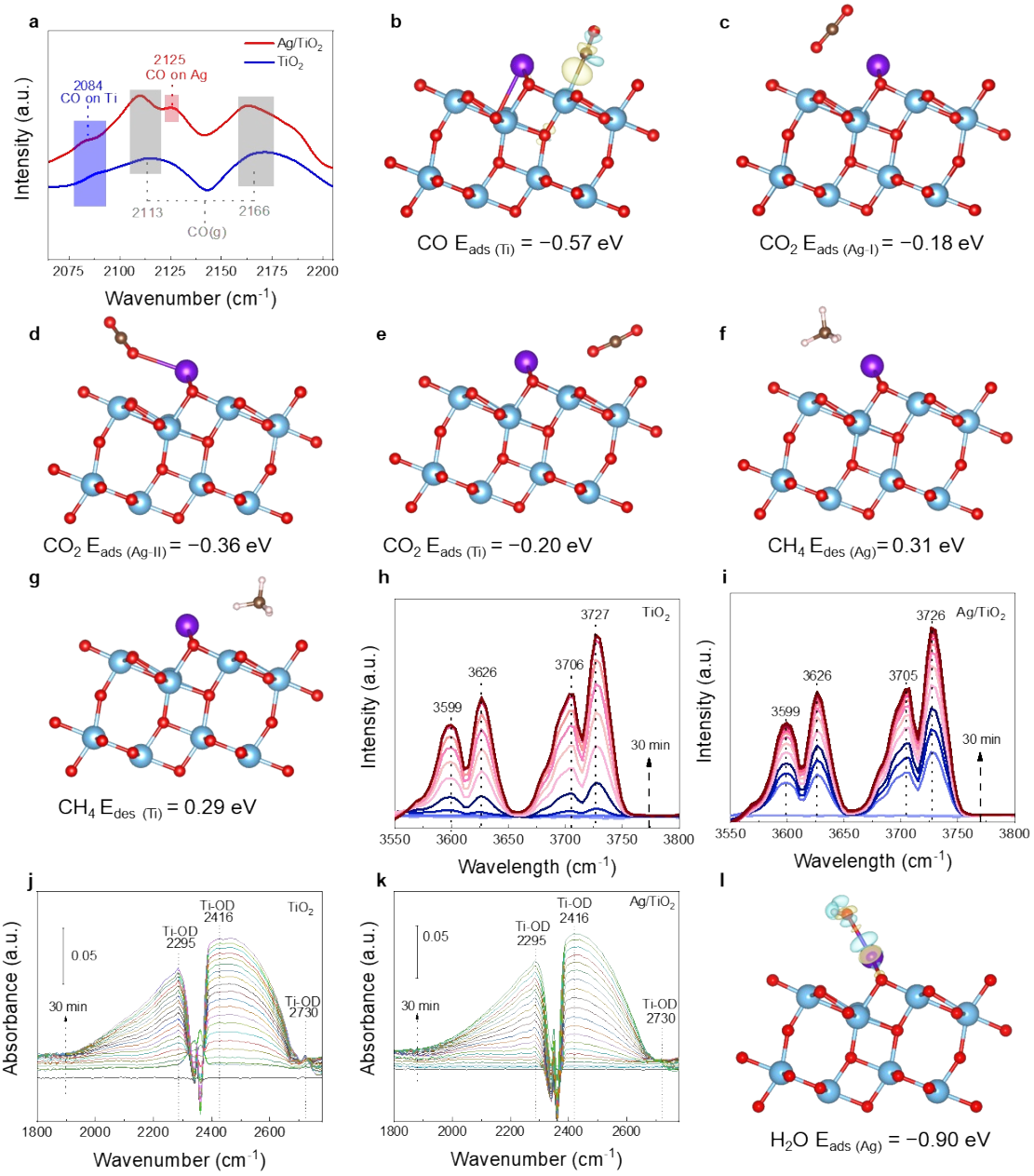

Supplementary Fig. S18. (**a**) CO-DRIFTS of TiO_2 and Ag/TiO_2. (**b**) Charge density difference of CO adsorption at the Ti site on Ag/TiO_2. Optimized adsorption configurations and the adsorption energy (E_{ad}) of CO_2 at the (**c-d**) Ag and (**e**) Ti site on $Ag/TiO_2(101)$, respectively. Optimized adsorption configurations and desorption energy (E_{des}) of CH_4 at the (**f**) Ag and (**g**) Ti site on $Ag/TiO_2(101)$, respectively. E_{ad} is calculated as $E_{ad} = E_{X/surf} - E_{surf} - E_X$, in which $E_{X/surf}$ and E_{surf} are the total energies of the surface with and without an X (X = CO_2 and CH_4) adsorbed and E(X) is the total energy of an isolated X. E_{des} is calculated to be $E_{des} = E_{surf} + E_X - E_{X/surf}$. *In situ* DRIFTS co-adsorption of a mixture of CO_2 and H_2O vapor on (**h**) TiO_2 and (**i**) Ag/TiO_2. *In situ* DRIFTS for adsorption of D_2O vapor on (**j**) TiO_2 and (**k**) Ag/TiO_2. (**l**) Charge density difference of H_2O adsorption at the Ag site on Ag/TiO_2. The yellow and cyan color represents electron accumulation and depletion, respectively. The isosurface value is 2.5×10^{-3} e Å^{-3}. The blue, red and purple balls represent Ti, O and Ag atoms, respectively.

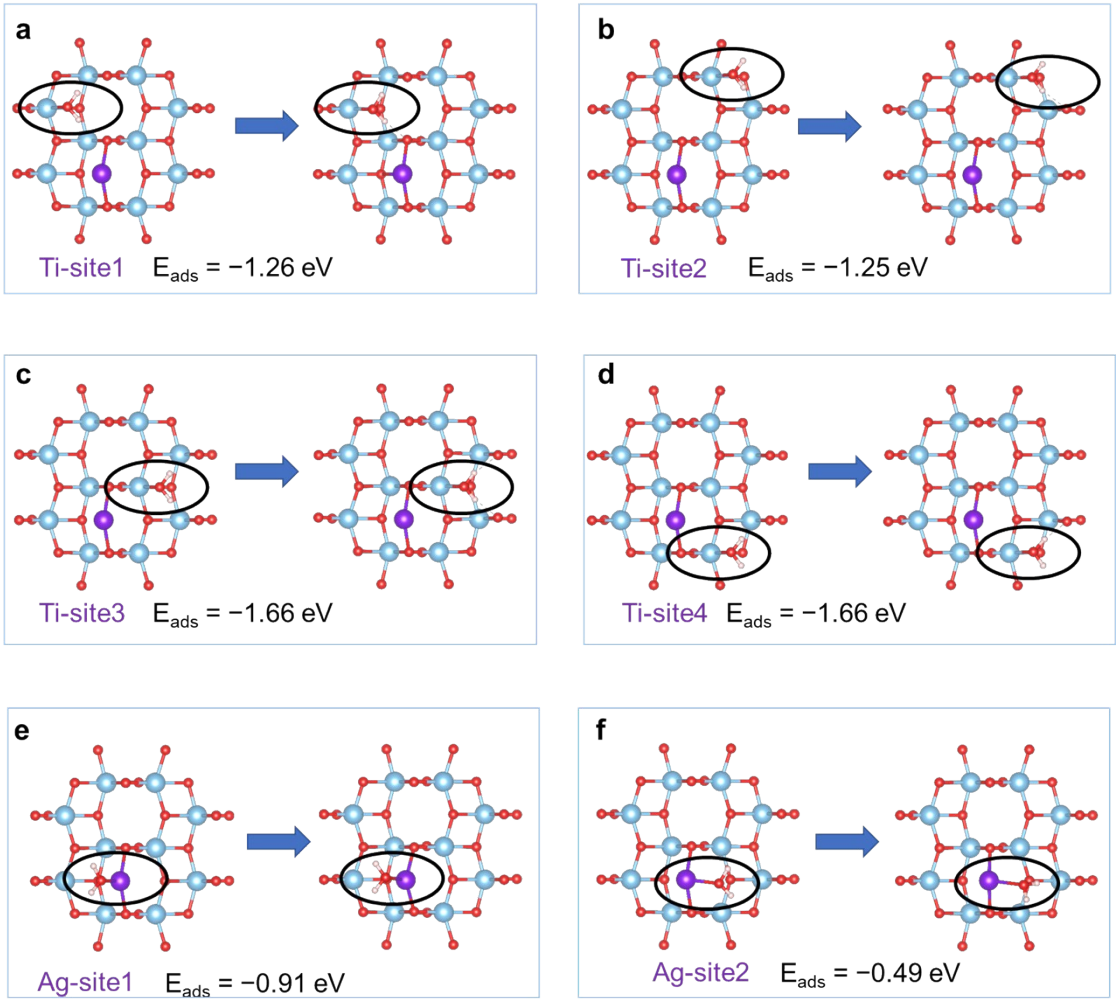

Supplementary Fig. S19. Possible inequivalent adsorption structures before (left panel) and after (right panel) relaxation as well as the corresponding adsorption energies of H_2O on Ag/TiO_2. The blue, red, purple and white balls represent Ti, O, Ag and H atoms, respectively.

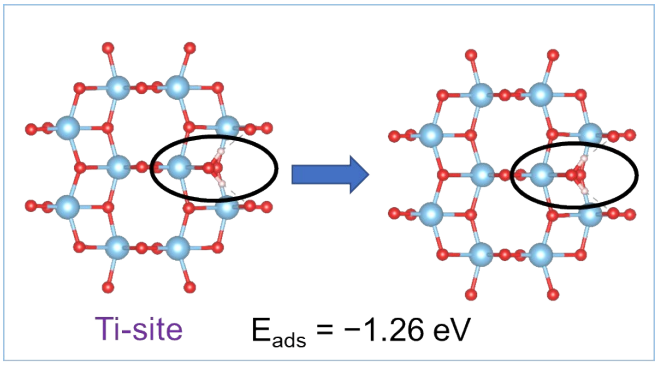

Supplementary Fig. S20. Adsorption structure before (left panel) and after (right panel) relaxation as well as the adsorption energy of H_2O on TiO_2. The blue, red and white balls represent Ti, O and H atoms, respectively.

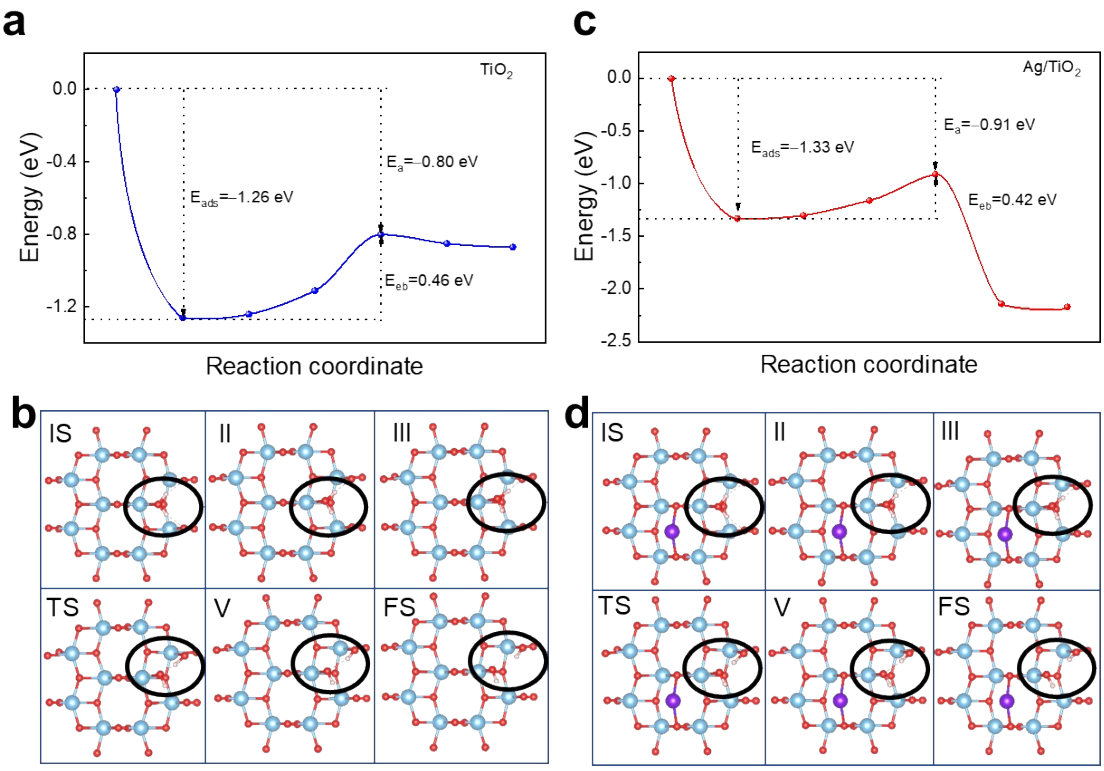

Supplementary Fig. S21. Potential energy surfaces of H_2O splitting on (**a**) TiO_2 and (**c**) Ag/ TiO_2. Corresponding structures at each state on (**b**) TiO_2 and (**d**) Ag/TiO_2. The blue, red, purple and white balls represent Ti, O, Ag and H atoms, respectively.

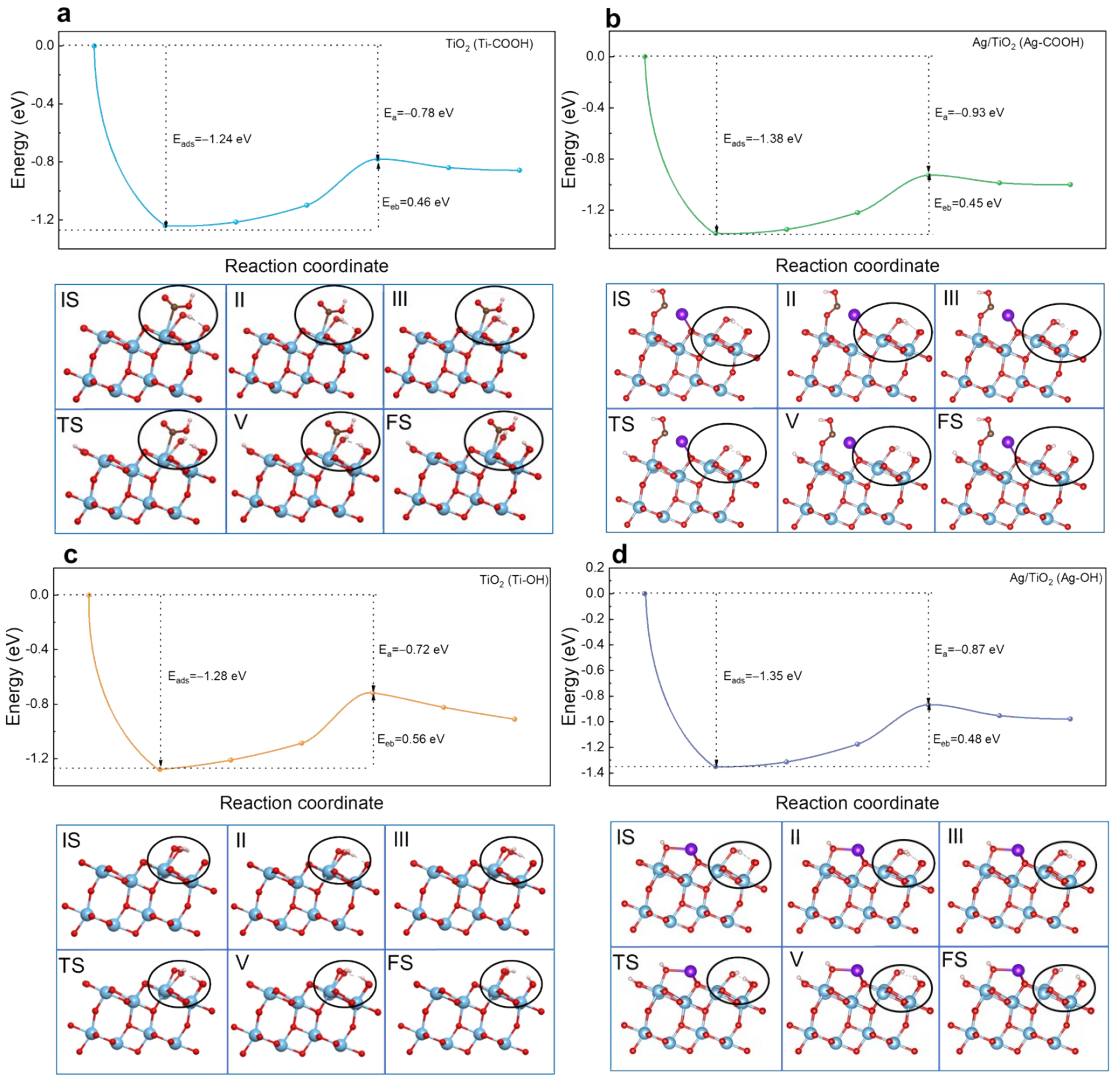

Supplementary Fig. S22. Potential energy surfaces of H_2O splitting on (**a**) TiO_2 and (**b**) Ag/TiO_2 with optimized configuration at each state when *COOH is adsorbed nearby. Potential energy surfaces of H_2O splitting on (**c**) TiO_2 and (**d**) Ag/TiO_2 with optimized configuration at each state when *OH is adsorbed nearby. The blue, red, purple and white balls represent Ti, O, Ag and H atoms, respectively.

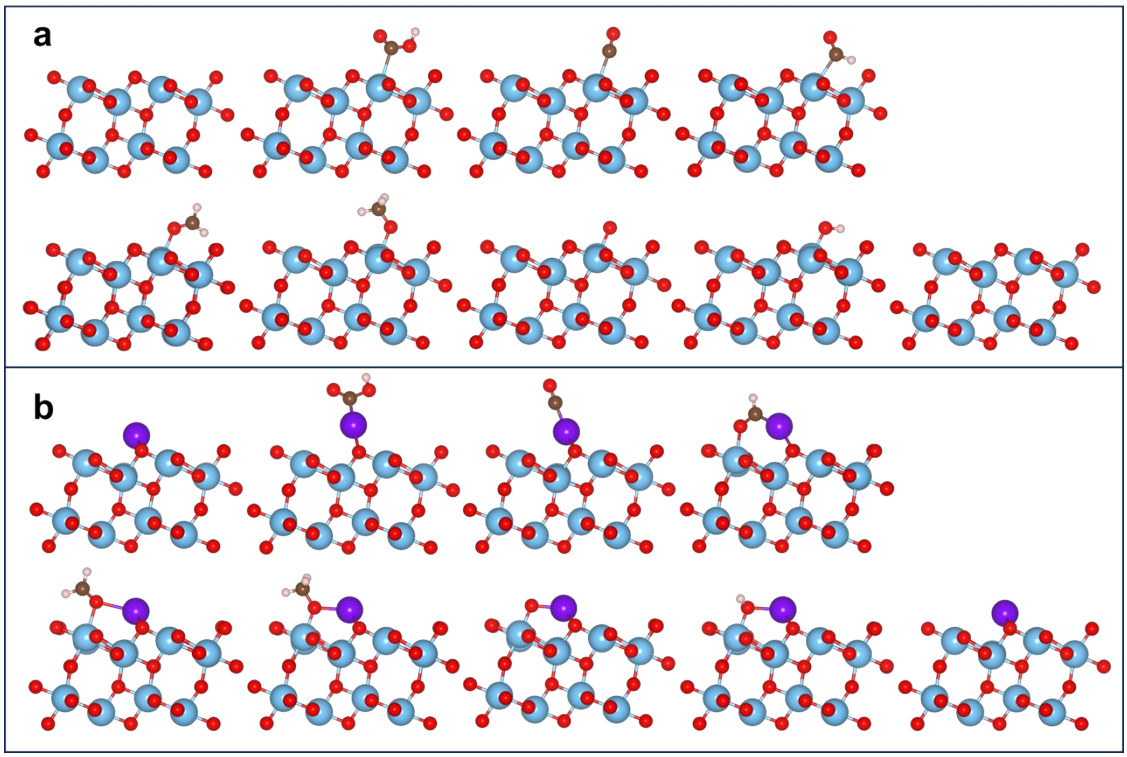

Supplementary Fig. S23. The optimized adsorption structure of CO_2 reduction to CH_4 on (**a**)TiO_2 and (**b**) Ag/TiO_2. The blue, red, purple, brown and white balls represent Ti, O, Ag, C and H atoms, respectively.

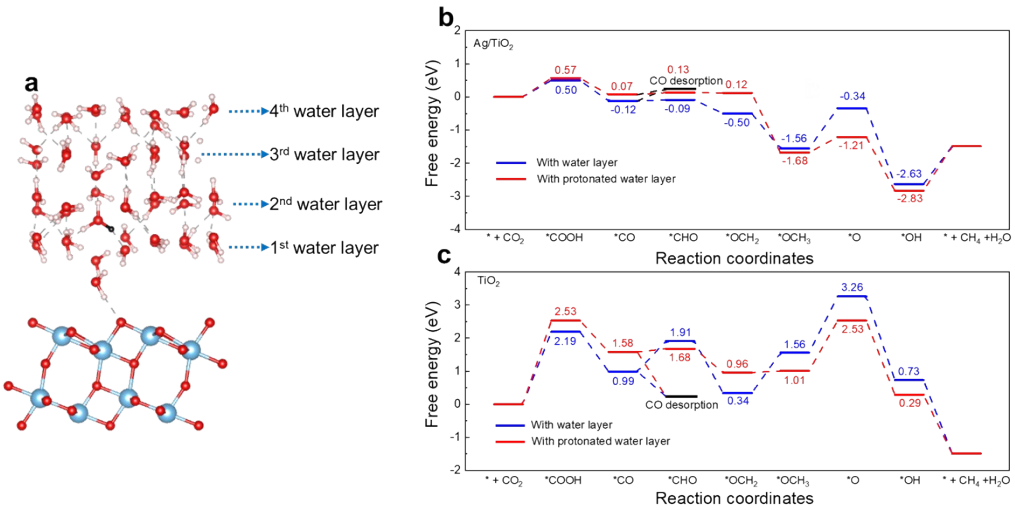

Supplementary Fig. S24. (**a**) Side views of protonated water layer structure on TiO_2(101). The blue, red, white and black balls represent Ti, O, H and the extra proton, respectively. Free energy diagrams of photocatalytic CO_2 methanation on (**b**) TiO_2 and (**c**) Ag/TiO_2 with and without an extra proton in the water layers.

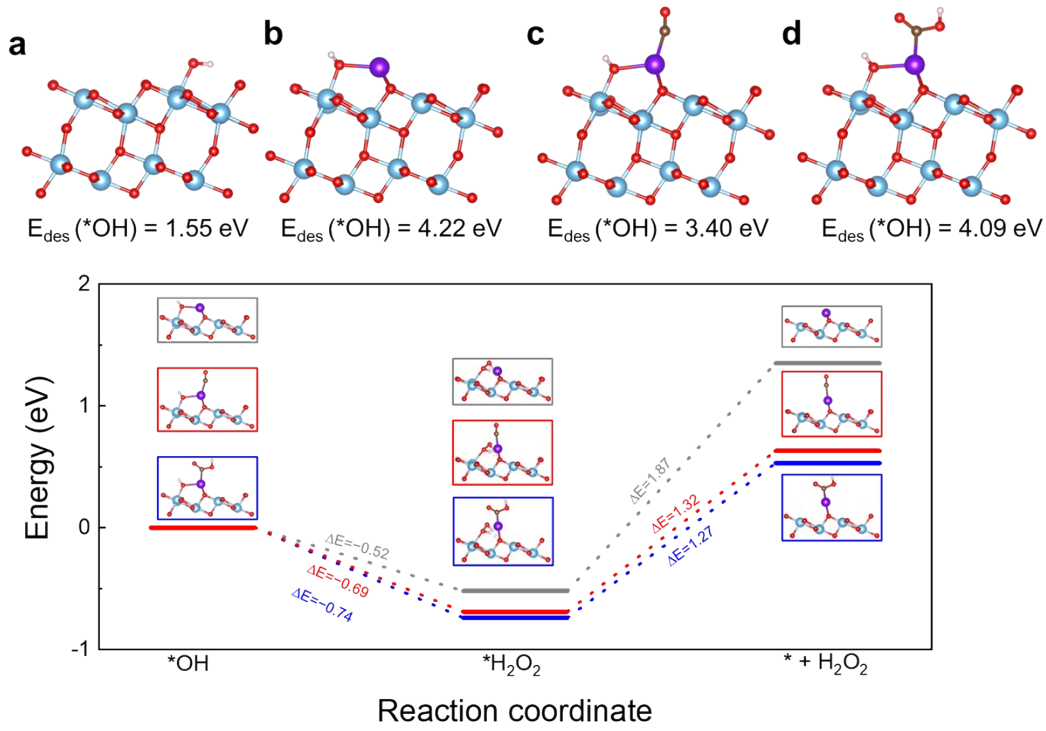

Supplementary Fig. S25. Optimized adsorption configurations and desorption energy (E_{des}) of *OH to form an •OH from (**a**) TiO_2(101) and (**b**) Ag/TiO_2(101) as well as Ag/TiO_2(101) with a (**c**) *CO or (**d**) *COOH adsorbed at the Ag site. E_{des} is calculated to be $E_{des} = E_{surf} + E_{•OH} - E_{*OH/surf}$. $E_{*OH/surf}$ and E_{surf} are the total energies of the surface with and without an *OH adsorbed and $E_{•OH}$ is the total energy of an isolated •OH. (**e**) The energy profiles for *OH desorption from Ag/TiO_2(101) via the path of *OH + •OH → *H_2O_2 → * + H_2O_2 with optimized structures at each state. The gray, red and blue lines indicate the process on pristine Ag/TiO_2(101) and that on Ag/TiO_2(101) with an adjacent *CO or *COOH, respectively. The blue, red, purple white and brown balls represent Ti, O, Ag, C and H atoms, respectively.

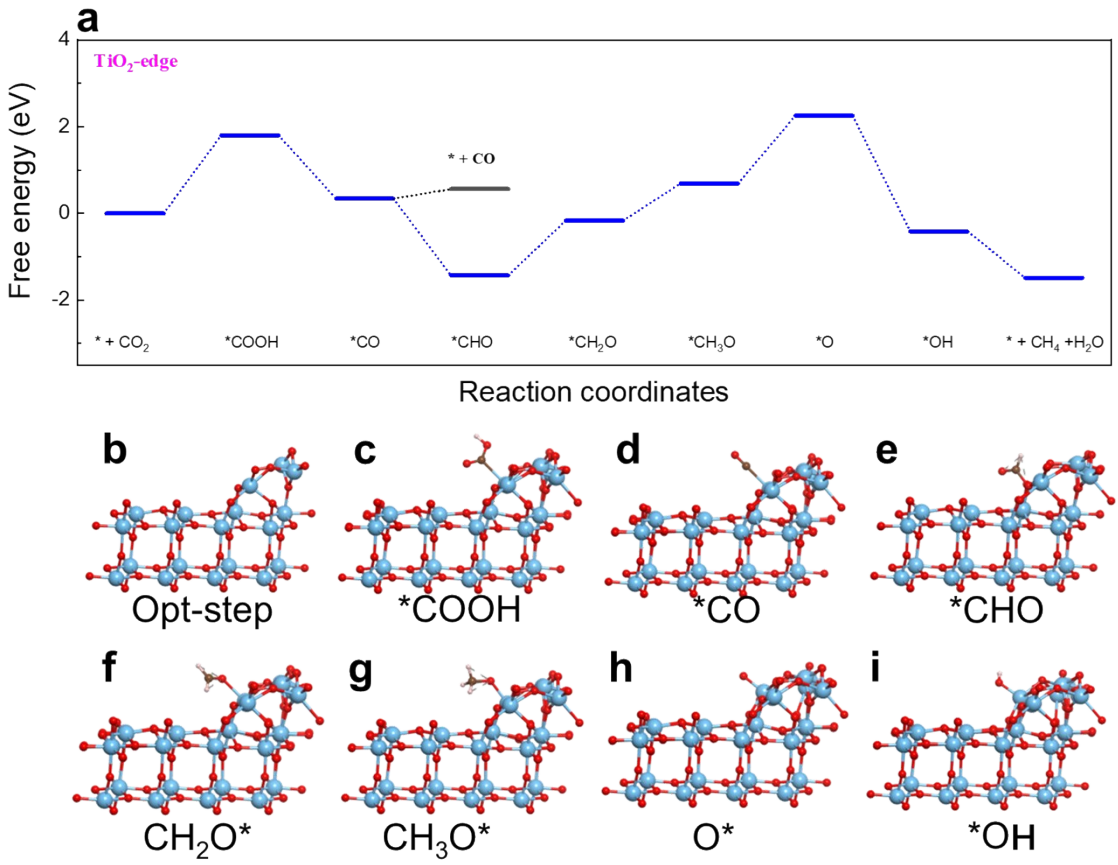

Supplementary Fig. S26. Free energy diagrams (**a**) of photocatalytic CO_2 methanation and corresponding optimized structure (**b-i**) at each state on step of TiO_2.

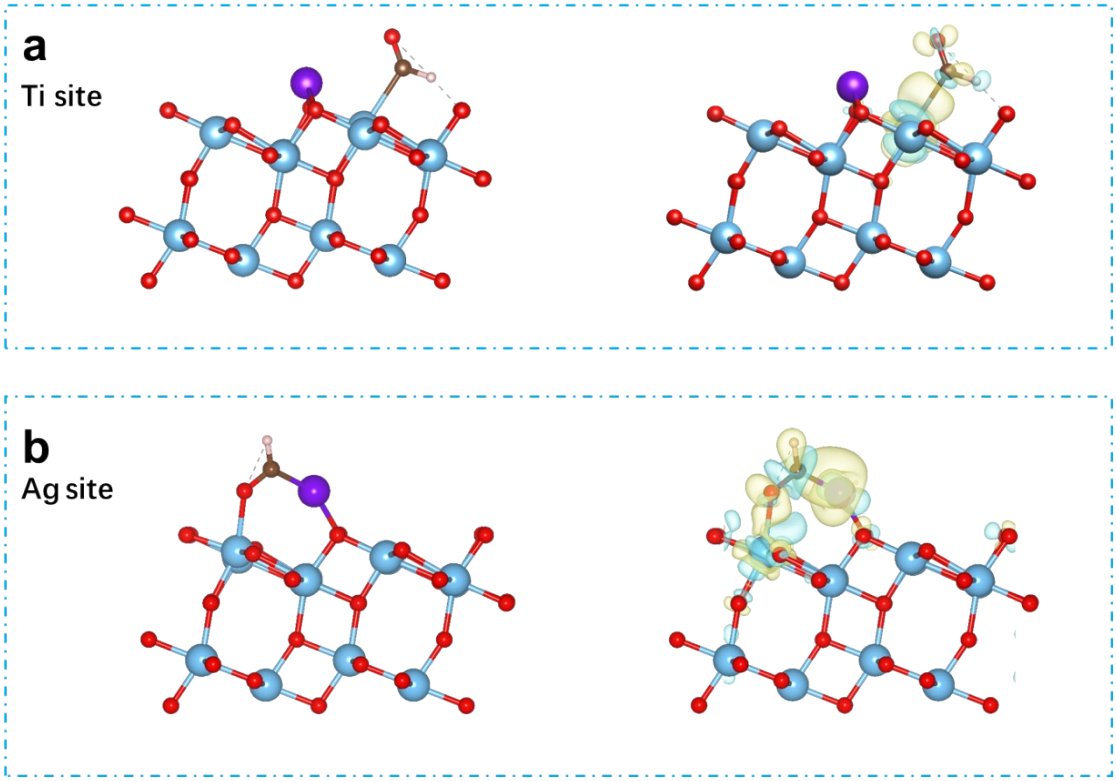

Supplementary Fig. S27. The adsorption configurations (left panel) and corresponding charge density difference (right panel) of *CHO at the (**a**) Ti and (**b**) Ag site. The yellow and cyan color represents electron accumulation and depletion, respectively. The isosurface value is 2.5 × 10^{-3} e $Å^{-3}$. The blue, red, purple and white balls represent Ti, O, Ag and H atoms, respectively.

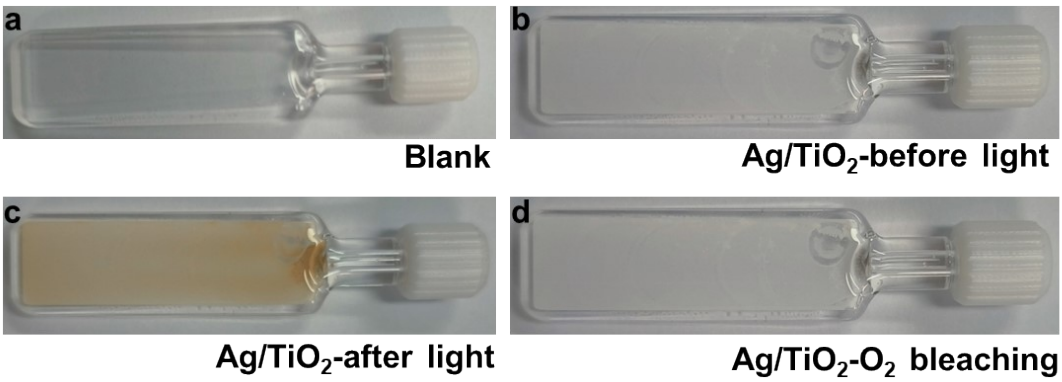

Supplementary Fig. S28. (**a**) The empty screw-top cuvette. The screw-top cuvette containing sample (**b**) before irradiation, (**c**) after irradiation and (**d**) after O_2 bleaching.

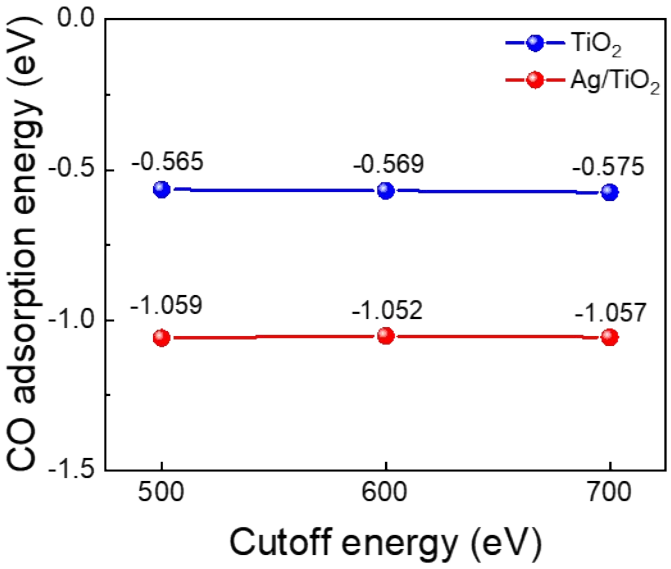

Supplementary Fig. S29. Testing calculations about cutoff energy: the adsorption energies of CO on TiO_2(101) and Ag/TiO_2(101).

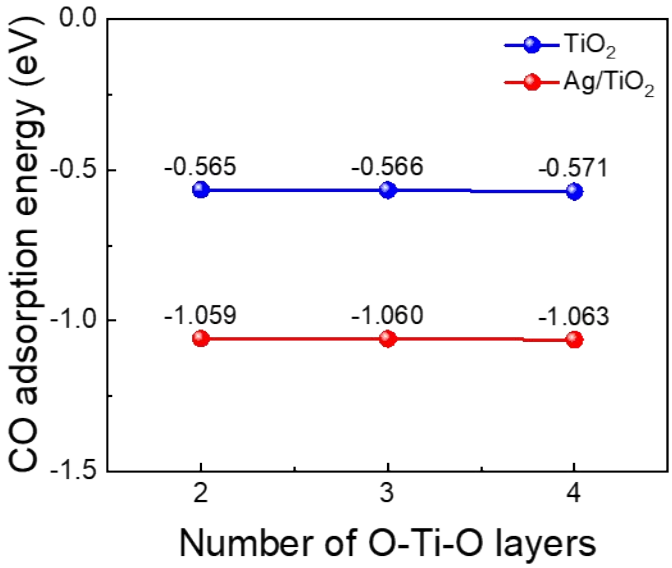

Supplementary Fig. S30.Testing calculations about the number of O-Ti-O layer used in the systems: the adsorption energies of CO on TiO_2(101) and Ag/TiO_2(101).

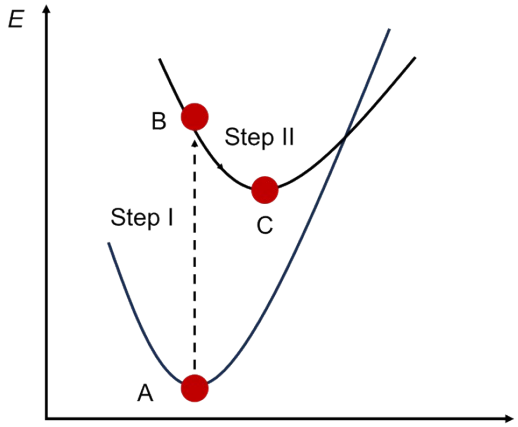

Supplementary Fig. S31. Procedures of calculating electron excitation via occupation-constrained DFT.

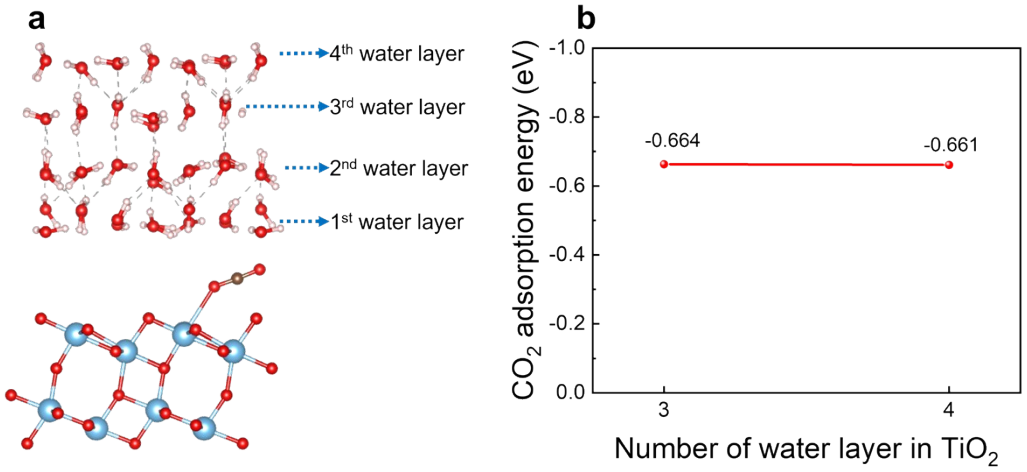

Supplementary Fig. S32. Testing calculations about the number of water layers in the simulation of explicit water solvation. (**a**) Side views of water layer structure on TiO_2(101). The blue, red, white and black balls represent Ti, O, H and the extra proton, respectively. (**b**) Adsorption energy of CO_2 on TiO_2.

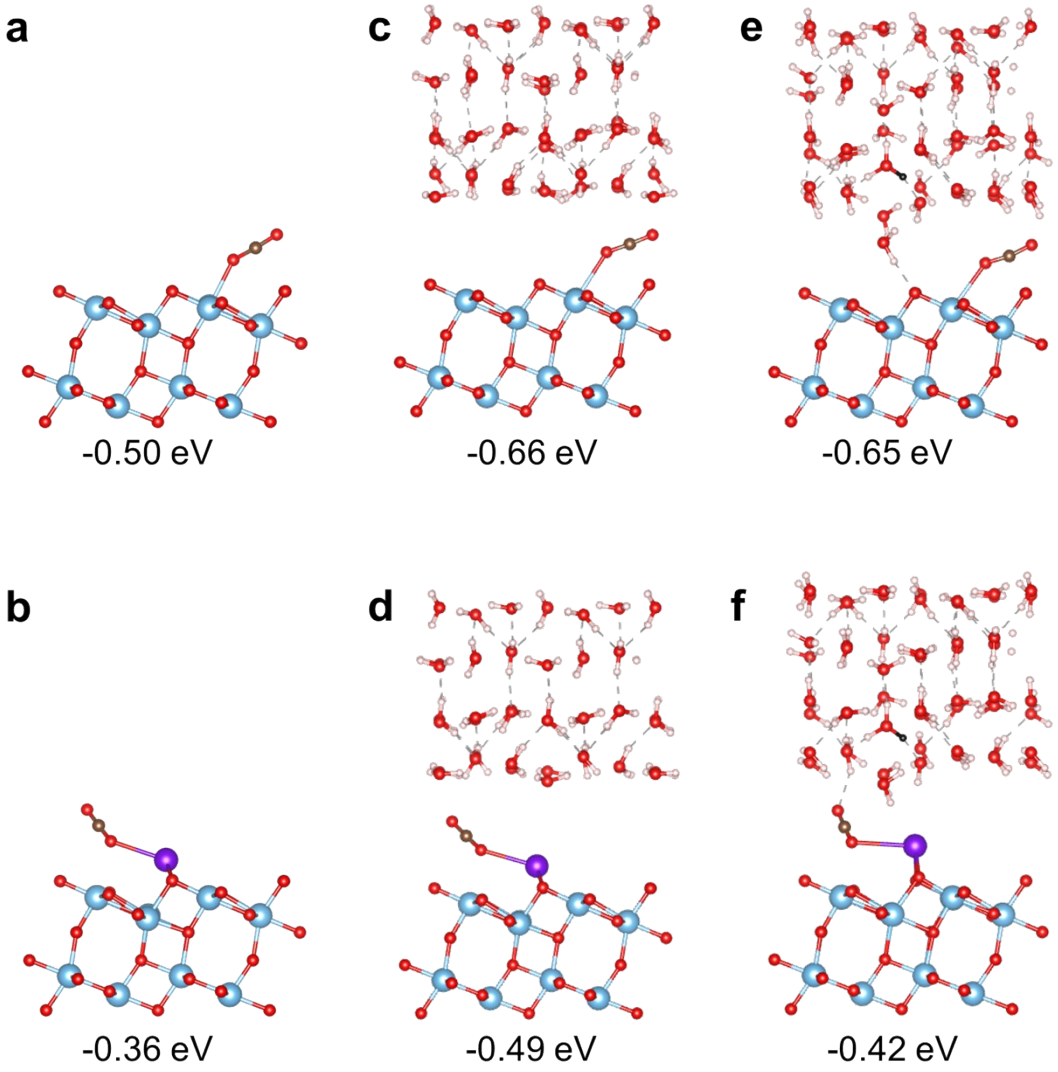

Supplementary Fig. S33. Adsorption energies and configurations of CO_2 on TiO_2 (upper panels) and Ag/TiO_2 (lower panels): (**a, b**) in the absence of water layers, (**c, d**) in the presence of water layers and (**e, f**) in the presence of protonated water layers. The blue, red, purple, white and black balls represent Ti, O, Ag, H and the extra proton, respectively.

Supplementary Table S1. The least-squares FT-EXAFS fitting quantification structural parameters of Ag_2O, Ag and Ag/TiO_2.

Sample	Shell	[a]*N*	[b]*R* (Å)	[c]σ^2 (Å^2)	[d]ΔE_0 (eV)	*R* factor (%)
Ag foil	Ag-Ag	12*	2.86±0.002	0.0096	0.57±0.28	0.4
Ag_2O	Ag-O	2*	2.06±0.017	0.0037	5.86±1.99	0.7
Ag/TiO_2	Ag-O	2.1±0.2	2.02±0.004	0.0054	8.53±1.40	1.4

[a]*N*: coordination numbers; [b]*R*: bond distance; [c]σ^2: Debye-Waller factors; [d]ΔE_0: the inner potential correction. *R* factor: the goodness of fit.

S_0^2 was set as 0.8 for Ag data, which was obtained from the experimental EXAFS fit of Ag foil, reference by fixing coordination numbers as the known crystallographic value and was fixed to all the samples.

Supplementary Table S2. Pore diameter and surface area of TiO_2 and Ag/TiO_2.

Samples	Pore diameter (nm)	Surface area (m^2 g^{-1})
Ag/TiO_2	11.85	45.08
TiO_2	11.75	57.46

Supplementary Table S3. The photogenerated charge lifetime (τ_1, τ_2 and τ_{ave}) of samples.

Samples	τ_1 (ns)	τ_2 (ns)	τ_{ave} (ns)
TiO_2	2.2164	40.5443	35.4473
Resting-state Ag/TiO_2	1.7376	38.5879	32.8774
Active-state Ag/TiO_2	1.2828	26.9329	15.4931

Supplementary Table S4. Comparison of photocatalytic CO_2 reduction yield and CH_4 selectivity of various noble metal supported catalysts.

Materials	Product and yield (μmol g^{-1} h^{-1})	Electron selectivity for CH_4 (%)	Ref.
Ag/TiO_2	**CO 18.4, CH_4 46.0**	**91**	**this work**
$Cu/Au/Al_2O_3/p\text{-}GaN$	CO 600	0	S41[41]
IrQPY/CoPc	CO 40	0	S42[42]
Co $Ru/g\text{-}C_3N_4$	CO 27.3	0	S43[43]
TiO_2/AC-5-Ag	CO 0.91	0	S44[44]
Ag/TiO_2	CO 0.575	0	S45[45]
Au_c-C-Co	H_2 1.539 CO 3.451, CH_4 0.075	6	S46[46]
$Au/g\text{-}C_3N_4$	CO 28.3, CH_4 1.3	16	S47[47]
$Pd/g\text{-}C_3N_4$	CH_3OH 3.17, CH_4 0.4	34	S48[48]
$Au/TiO_2(O)$	CO 25.9, CH_4 5.3	45	S49[49]
Au/CdS	H_2 7.9, CO 32.2, CH_4 11.3	53	S50[50]
$Au/g\text{-}C_3N_4$	CO 9.729, CH_4 4.8	66	S51[51]
1.5Ag Nanoparticles/TiO_2	CO 0.7, CH_4 5.8	97	S52[52]
$Pd/g\text{-}C_3N_4$	CO 0.46, CH_4 20.3	99	S53[53]
$1.0Pt/In_2O_3$	CO 8.6, CH_4 21.0	91	S54[54]
Pt_n/3DOM-$SrTiO_3$	CO 4.1, CH_4 26.7	96	S55[55]
$Au/TiO_2/W_{18}O_{49}$	CO 2.57, CH_4 35.55	98	S56[56]
$PtRu/TiO_2$	H_2 16.8, CO 2.6, CH_4 38.7	89	S57[57]
Pd-TiO_2	CO 34, CH_4 48	85	S58[58]
Ag/TiO_2	CO 205, CH_4 100	66	S59[59]
Pd Nanoparticles/TiO_2	CH_4 237.4	100	S60[60]

Supplementary Notes 1: The carrier migration rates and migration efficiencies are calculated as follows:[61, 62]

$$\text{Carrier migration rates } k = \frac{1}{\tau_{ave}(\text{modified})} - \frac{1}{\tau_{ave}(\text{bare})} \quad (1)$$

$$\text{Carrier migration efficiencies } \eta = 1 - \frac{\tau_{ave}(\text{modified})}{\tau_{ave}(\text{bare})} \quad (2)$$

Supplementary Notes 2: Photocatalytic CO_2 reduction mechanism on TiO_2 and Ag/TiO_2.

$CO_2(g) + H_2O \rightarrow 2H^+ + CO_3^{2-}$ (1)

$* + CO_2(g) \rightarrow *CO_2$, or $* + 2H^+ + CO_3^{2-} \rightarrow H_2O + *CO_2$ (2)

$* CO_2 + e^- + H^+ \rightarrow *COOH$ (3)

$*COOH + H^+ + e^- \rightarrow *CO + H_2O$ (4)

$*CO + H^+ + e^- \rightarrow *CHO$, or $*CO \rightarrow CO(g) + *$ (5)

$*CHO + H^+ + e^- \rightarrow *OCH_2$ (6)

$*OCH_2 + H^+ + e^- \rightarrow *OCH_3$ (7)

$*OCH_3 + H^+ + e^- \rightarrow *CH_4 + O*$ (8)

$*CH_4 + *O + H^+ + e^- \rightarrow CH_4(g) + *OH$ (9)

$*OH + H^+ + e^- \rightarrow H_2O*$ (10)

$H_2O* \rightarrow H_2O + *$ (11)

Reference:

1. B. Ravel and M. Newville, *J. Synchrotron. Radiat.*, 2005, **12**, 537-541.
2. J. J. Rehr and R. C. Albers, *Rev. Mod. Phys.*, 2000, **72**, 621-654.
3. D. C. Koningsberger and R. Prins, X-ray absorption: principles, applications, techniques of EXAFS, SEXAFS and XANES, *John Wiley & Sons Ltd.*, Chichester, 1988.
4. G. Kresse and J. Furthmuller, *Phys. Rev. B*, 1996, **54**, 11169-11186.
5. G. Kresse and J. Furthmuller, *Comp. Mater. Sci.*, 1996, **6**, 15-50.
6. P. E. Blochl, O. Jepsen and O. K. Andersen, *Phys. Rev. B* 1994, **49**, 16223-16233.
7. J. P. Perdew, K. Burke and M. Ernzerhof, *Phys. Rev. Lett.*, 1996, **77**, 3865-3868.
8. T. P. Senftle, M. Lessio and E. A. Carter, *Chem. Mater.*, 2016, **28**, 5799-5810.
9. X. L. Zheng, B. Zhang, P. De Luna, Y. F. Liang, R. Comin, O. Voznyy, L. L. Han, F. P. Garcia de Arquer, M. Liu, C. T. Dinh, T. Regier, J. J. Dynes, S. S. He, H. L. Xin, H. S. Peng, D. Prendergast, X. W. Du and E. H. Sargent, *Nat. Chem.*, 2018, **10**, 149-154.
10. W. G. Chen, P. F. Yuan, S. Zhang, Q. Sun, E. J. Liang and Y. Jia, *Physica B*, 2012, **407**, 1038-1043.
11. J. Bang, Z. Wang, F. Gao, S. Meng and S. B. Zhang, *Phys. Rev. B*, 2013, **87**, 205206.
12. X. B. Li, X. Q. Liu, X. Liu, D. Han, Z. Zhang, X. D. Han, H. B. Sun and S. B. Zhang, *Phys. Rev. Lett.*, 2011, **107**, 015501.
13. H. Pfau, R. Daou, S. Friedemann, S. Karbassi, S. Ghannadzadeh, R. Kuchler, S. Hamann, A. Steppke, D. Sun, M. Konig, A. P. Mackenzie, K. Kliemt, C. Krellner and M. Brando, *Phys. Rev. Lett.*, 2017, **119**, 126402.
14. S. A. Trygubenko and D. J. Wales, *J. Chem. Phys.*, 2004, **120**, 2082-2094.
15. J. K. Nørskov, J. Rossmeisl, A. Logadottir and L. Lindqvist, *J. Phys. Chem. B*, 2004, **108**, 17886.
16. J. K. Norskov, J. Rossmeisl, A. Logadottir, L. Lindqvist, J. R. Kitchin, T. Bligaard and H. Jonsson, *J. Phys. Chem. B*, 2004, **108**, 17886-17892.
17. J. Q. Xu, Z. Y. Ju, W. Zhang, Y. Pan, J. F. Zhu, J. W. Mao, X. L. Zheng, H. Y. Fu, M. L. Yuan, H. Chen and R. X. Li, *Angew. Chem. Int. Ed.*, 2021, **60**, 8705-8709.
18. N. Q. Zhang, X. X. Zhang, L. Tao, P. Jiang, C. L. Ye, R. Lin, Z. W. Huang, A. Li, D. W. Pang, H. Yan, Y. Wang, P. Xu, S. F. An, Q. H. Zhang, L. C. Liu, S. X. Du, X. D. Han, D.

S. Wang and Y. D. Li, *Angew. Chem. Int. Ed.*, 2021, **60**, 6170-6176.

19. M. W. Chase, J. L. Curnutt, J. R. Downey, R. A. McDonald, A. N. Syverud and E. A. Valenzuela, *J. Phys. Refe. Data*, 1982, **11**, 695-940.

20. C. G. Ban, Y. Wang, J. P. Ma, Y. J. Feng, J. J. Ding, Y. Y. Duan, X. Liu, B. Zhang, J. J. Tang, X. P. Tao, L. Y. Gan, S. S. Tan and X. Y. Zhou, *Sep. Purif. Technol.*, 2023, **326**, 124745.

21. S. Karmakar, S. Barman, F. A. Rahimi, S. Biswas, S. Nath and T. K. Maji, *Energ. Environ. Sci.*, 2023, **16**, 2187-2198.

22. B. H. Lee, E. H. Gong, M. H. Kim, S. H. Park, H. R. Kim, J. H. Lee, E. Y. Jung, C. W. Lee, J. S. Bok, Y. O. Jung, Y. S. Kim, K. S. Lee, S. P. Cho, J. W. Jung, C. H. Cho, S. Lébegue, K. T. Nam, H. J. Kim, S. L. In and T. Hyeon, *Energ. Environ. Sci.*, 2021, **15**, 601-609.

23. J. Li, H. L. Huang, W. J. Xue, K. Sun, X. H. Song, C. R. Wu, L. Nie, Y. Li, C. Y. Liu, Y. Pan, H. L. Jiang, D. H. Mei and C. L. Zhong, *Nat. Catal.*, 2021, **4**, 719-729.

24. X. D. Li, Y. F. Sun, J. Q. Xu, Y. J. Shao, J. Wu, X. L. Xu, Y. Pan, H. X. Ju, J. F. Zhu and Y. Xie, *Nat. Energy*, 2019, **4**, 690-699.

25. Z. q. Wang, J. c. Zhu, X. l. Zu, Y. Wu, S. Shang, P. Q. Ling, P. Z. Qiao, C. Y. Liu, J. Hu, Y. Pan, J. F. Zhu, Y. F. Sun and Y. Xie, *Angew. Chem. Int. Ed.* , 2022, **61**, e202203249.

26. H. Z. Yang, D. R. Yang, Y. Zhou and X. Wang, *J. Am. Chem. Soc.*, 2021, **143**, 13721-13730.

27. S. K. Yin, X. X. Zhao, E. H. Jiang, Y. Yan, P. Zhou and P. W. Huo, *Energ. Environ. Sci.*, 2022, **15**, 1556-1562.

28. J. Zhou, J. Li, L. Kan, L. Zhang, Q. Huang, Y. Yan, Y. F. Chen, J. Liu, S. L. Li and Y. Q. Lan, *Nat. Commun.*, 2022, **13**, 4681.

29. K. Jiang, R. B. Sandberg, A. J. Akey, X. Y. Liu, D. C. Bell, J. K. Nørskov, K. Chan and H. T. Wang, *Nat. Catal.*, 2018, **1**, 111-119.

30. J. Rossmeisl, E. Skúlason, M. E. Björketun, V. Tripkovic and J. K. Nørskov, *Chem. Phys. Lett.*, 2008, **466**, 68-71.

31. Y. Wang, X. P. Qin and M. H. Shao, *J. Catal.*, 2021, **400**, 62-70.

32. A. B. Munoz-Garcia and E. A. Carter, *J. Am. Chem. Soc.*, 2012, **134**, 13600-13603.

33. G. P. Hao, W. C. Li, D. Qian and A. H. Lu, *Adv. Mater.*, 2010, **22**, 853-8537.

34. L. f. Wang and R. T. Yang, *J. Phys. Chem. C*, 2011, **116**, 1099-1106.

35. Z. Yan, J. L. Hitt, Z. Zeng, M. A. Hickner and T. E. Mallouk, *Nat. Chem.*, 2021, **13**, 33-40.

36. N. Wang, Y. C. Feng, X. Guo and A. C. T. van Duin, *J. Phys. Chem. C*, 2018, **122**, 21401-21410.

37. A. Özgür Yazaydın, A. I. Benin, S. A. Faheem, P. Jakubczak, J. J. Low, R. R. Willis and R. Q. Snurr, *Chem. Mater.*, 2009, **21**, 1425–1430.

38. H. J. Zhu, W. J. Xue, H. L. Huang, L. Y. Chen, H. Y. Liu and C. L. Zhong, *Nano Res.*, 2022, **16**, 6113-6119.

39. J. Hussain, H. Jónsson and E. Skúlason, *ACS Catal.*, 2018, **8**, 5240-5249.

40. Á. B. Höskuldsson, E. Tayyebi and E. Skúlason, *J. Catal.*, 2021, **404**, 362-370.

41. R. G. Li, W. H. Cheng, M. H. Richter, J. S. DuChene, W. m. Tian, C. Li and H. A. Atwater, *ACS Energy Lett.*, 2021, **6**, 1849-1856.

42. J. W. Wang, L. Jiang, H. H. Huang, Z. Han and G. Ouyang, *Nat. Commun.*, 2021, **12**, 4276.

43. L. Cheng, X. Y. Yue, L. X. Wang, D. N. Zhang, P. Zhang, J. J. Fan and Q. J. Xiang, *Adv. Mater.*, 2021, **33**, e2105135.

44. Z. Y. Jiang, X. H. Zhang, Z. M. Yuan, J. C. Chen, B. B. Huang, D. D. Dionysiou and G. H. Yang, *Chem. Eng. J.*, 2018, **348**, 592-598.

45. G. H. Li, Y. Y. Sun, Q. M. Zhang, Z. H. Gao, W. Sun and X. X. Zhou, *Chem. Eng. J.*, 2021, **410**, 128397.

46. X. F. Cui, J. Wang, B. Liu, S. Ling, R. Long and Y. J. Xiong, *J. Am .Chem. Soc.*, 2018, **140**, 16514-16520.

47. F. Li, H. P. Zhou, J. J. Fan and Q. J. Xiang, *J. Colloid. Interf. Sci.*, 2020, **570**, 11-19.

48. S. W. Cao, Y. Li, B. C. Zhu, M. Jaroniec and J. G. Yu, *J. Catal.*, 2017, **349**, 208-217.

49. A. Wang, S. J. Wu, J. L. Dong, R. X. Wang, J. W. Wang, J. L. Zhang, S. X. Zhong and S. Bai, *Chem. Eng. J.*, 2021, **404**, 127145.

50. Y. H. Cao, L. Guo, M. Dan, D. E. Doronkin, C. Q. Han, Z. Q. Rao, Y. Liu, J. Meng, Z. A. Huang, K. B. Zheng, P. Chen, F. Dong and Y. Zhou, *Nat. Commun.*, 2021, **12**, 1675.

51. X. Li, C. Y. Liu, D. Y. Wu, J. Z. Li, P. W. Huo and H. Q. Wang, *Chinese J. Catal.*, 2019, **40**, 928-939.

52. L. Collado, A. Reynal, F. Fresno, M. Barawi, C. Escudero, V. Perez-Dieste, J. M. Coronado, D. P. Serrano, J. R. Durrant and V. A. de la Pena O'Shea, *Nat. Commun.*, 2018, **9**, 4986.

53. P. G. Liu, Z. X. Huang, X. P. Gao, X. Hong, J. F. Zhu, G. M. Wang, Y. E. Wu, J. Zeng and X. S. Zheng, *Adv. Mater.*, 2022, **34**, e2200057.

54. Y. J. Ma, X. X. Yi, S. L. Wang, T. Li, B. Tan, C. C. Chen, T. Majima, E. R. Waclawik, H. Y. Zhu and J. Y. Wang, *Nat. Commun.*, 2022, **13**, 1400.

55. X. X. Wu, C. J. Wang, Y. C. Wei, J. Xiong, Y. L. Zhao, Z. Zhao, J. Liu and J. M. Li, *J. Catal.*, 2019, **377**, 309-321.

56. X. Y. Jiang, J. D. Huang, Z. H. Bi, W. J. Ni, G. Gurzadyan, Y. G. Zhu and Z. Y. Zhang, *Adv .Mater.*, 2022, **34**, e2109330.

57. Y. C. Wei, X. X. Wu, Y. L. Zhao, L. Wang, Z. Zhao, X. T. Huang, J. Liu and J. M. Li, *Appl. Catal. B Environ.*, 2018, **236**, 445-457.

58. Y. B. Wang, J. Zhao, Y. X. Li and C. Y. Wang, *Appl. Catal. B Environ.*, 2018, **226**, 544-553.

59. H. N. Huang, R. Shi, Z. H. Li, J. Q. Zhao, C. L. Su and T. R. Zhang, *Angew. Chem. Int. Ed.*, 2022, **134**, e202200802.

60. Z. Zhan, H. Wang, Q. Huang, S. Q. Li, X. X. Yi, Q. Tang, J. Y. Wang and B. E. Tan, *Small*, 2022, **18**, e2105083.

61. Y. H. Li, M. L. Gu, X. M. Zhang, J. J. Fan, K. L. Lv, S. A. C. Carabineiro and F. Dong, *Mater. Today*, 2020, **41**, 270-303.

62. C. G. Ban, Y. Y. Duan, Y. Wang, J. P. Ma, K. W. Wang, J. Z. Meng, X. Liu, C. Wang, X. D. Han, G. Z. Cao, L. Y. Gan and X. Y. Zhou, *Nano-Micro Lett.*, 2022, **14**, 74.